Master in Bioengineering

Biological Engineering

Continuous synthesis of hydroxyapatite nanoparticles in a planar oscillatory flow reactor: Effect of surfactant concentration

Master dissertation

of

Joana Margarida Rodrigues de São João Machado

Developed within the course of dissertation

held in

FEUP/LEPABE

Supervisor: **Dr. António Ferreira**

Co-Supervisor: **Drª. Filipa Castro**

Chemical Engineering Department

July 2022

Agradecimentos/Ackowledgments

Ao Doutor António Ferreira e à Doutora Filipa Castro por me terem acolhido no grupo de investigação, pela orientação exemplar e disponibilidade durante este ano letivo, tanto durante o projeto de investigação, como durante a realização desta dissertação.

Ao meu namorado Álvaro pela compreensão, partilha e apoio durante o meu percurso académico.

Às minhas colegas Francisca e Inês pela interajuda, companheirismo e aventuras nestes últimos 6 anos juntas, em especial durante a escrita desta Dissertação.

Aos meus pais pelo apoio emocional (e financeiro) que me proporcionaram durante a minha vida académica, estiveram sempre lá para me apoiar, com as palavras certas para me manter motivada.

A todos,

Obrigada

This work was financially supported by LA/P/0045/2020 (ALiCE), UIDB/00511/2020 and UIDP/00511/2020 (LEPABE), funded by national funds through FCT/MCTES (PIDDAC).

Abstract

The crystallization/precipitation process plays a significant role in the pharmaceutical industry as it is the main purification process, of both intermediate compounds, and active pharmaceutical ingredients (API's). The quality of the mixture during crystallization plays a major role in controlling crystal characteristics, however, the crystallizers conventionally used in the industry are not capable of ensuring a uniform temperature and mixing control. The oscillatory flow reactor technology (OFR), offer several advantages to continuous perform crystallization/precipitation with high mixing control. The continuous synthesis of hydroxyapatite nanoparticles in a planar-OFR has been studied, due to its distinguished properties for medical applications. However some problems have been reported about the formation of particle aggregates in the suspension over time. In this study the effect of citrate to calcium ratio (Cit/Ca) on the dispersion/stability of HAp nanoparticles was evaluated during their continuous synthesis in a meso oscillatory flow reactor. The influence of flow rate and the scale-up of the reactor was also investigated, as well as an attempt to understand the mechanism of citrate on particle dispersion. The main goal of this work was the production of dispersed HAp nanoparticles in a meso-OFR (planar-OFC) with a precisely controlled particle size (<100nm) and a narrow size distribution, meeting the specific pharmaceutical requirements for drug delivery application. The samples were analysed by laser diffraction, Fourier-Transform Infrared Spectroscopy (FTIR) and Transmission Electron Microscopy (TEM). The zeta potential was measured to assess the suspension stability and the Ca/P molar ratio was also determined, total phosphorus in the powders was quantified by the ascorbic acid method and calcium was measured by atomic absorption spectroscopy.

This study confirmed the potential of citrate as a powerful tool to disperse the nanoparticles during its synthesis in a meso-OFR. The ratio of Cit/Ca=1.6 demonstrated to be the most efficient condition for particle dispersion, given the ability to obtain particle size distributions in the nanometric range, in the shortest amount of time. However it was possible to conclude that the flow rate and the residence time plays a significant role in the particle aggregation and in the apatite phase formation, respectively. The scale-up of the reactor did not reveal significant changes in the apatite phase obtained, neither in the suspension stability nor in the type of interactions occurring on the particle surface.

Keywords: hydroxyapatite, continuous crystallization, meso-oscillatory flow reactor, particle dispersion, sodium citrate

Resumo

O processo de cristalização/precipitação desempenha um papel importante na indústria farmacêutica por ser um dos principais processos de purificação de compostos intermédios e princípios ativos farmacêuticos (*API's*). Os cristalizadores tradicionalmente usados na indústria apresentam problemas na homogeneização da mistura dos reagentes, comprometendo assim o controlo das características dos cristais. O Reator de Fluxo Oscilatório (OFR) permite realizar a cristalização/precipitação em contínuo com alto grau de controlo da mistura. O estudo da síntese em contínuo de nanoparticulas de hidroxiapatite já foi realizado num meso-OFR (planar-OFC), tendo sido reportada a formação de agregados de partículas ao longo do tempo. Neste estudo, foi realizada a síntese em contituo de nanoparticulas de hidroxiapatite num meso-OFR (planar-OFC) com diferentes razões de citrato para cálcio (Cit/Ca), de modo a avaliar o seu efeito na dispersão/estabilidade da nanoparticulas produzias. Foi também avaliada a influência do caudal e do aumento de escala do reator, assim como uma tentativa de compreender o mecanismo do citrato na dispersão de partículas. O objetivo principal deste trabalho foi a produção de nanoparticulas de HAp assegurando o controlo do tamanho e distribuição das partículas (<100nm), de forma a corresponder aos requisitos específicos farmacêuticos para entrega de princípios ativos. As amostras foram analisadas por difração laser, Espetroscopia Infravermelha com Transformada de Fourier (FTIR) e Microscopia Eletrónica de Transmissão (TEM). O potencial zeta foi medido para avaliar a estabilidade da suspensão e a razão molar de cálcio para fósforo foi também determinada pela quantificação do fósforo total pelo método do ácido ascórbico e a do cálcio por espectroscopia de absorção atómica

Este estudo confirmou o potencial do citrato como ferramenta para a dispersão de nanoparticulas produzidas num meso-OFR. A razão de Cit/Ca=1.6 demonstrou ser a condição mais eficiente para a dispersão das partículas, dado a obtenção de partículas manométricas no menor período de tempo. Foi possível ainda concluir que o caudal e o tempo de residência também desempenham um papel crucial na dispersão de partículas e na formação da fase de apatite, respetivamente.

Palavras-Chave: hidroxiapatite, cristalização em contínuo, mesoreatores de fluxo oscilatório, dispersão de partículas, Citrato de sódio

Declaração

Declara, sob compromisso de honra, que este trabalho é original e que todas as contribuições não originais foram devidamente referenciadas com identificação da fonte.

4 de Julho de 2022

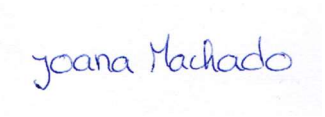

(Joana Machado)

Índex

List of Figures

List of Tables

Notation and Glossary

a	Activity	(M)
A	Pré-exponential factor	($m.kg^{3}.S^{-1}g^{-3}$)
C	Concentration in solution	($g.kg^{-1}$)
d	Diameter	(μm)
D	Internal tube diameter	(m)
f	Frequency of oscillation	(Hz)
g	Growth exponente	
G	Growth rate	($m.s^{-1}$)
J	Nucleation rate	($s^{-1}.L^{-1}$) ($min^{-1}L^{-1}$)
k_g	Constant of crystal growth	($m.kg^{g}.s^{-1}g^{-g}$)
L	Characteristic dimension	(m) (μm)
Q	Flow rate	($mL.min^{-1}$)
r	Cluster radius	(m)
r_c	Critical cluster radius	(m)
Re	Reynolds number	
Re_o	Oscillatory Reynolds number	
S	Supersaturation ratio	
St	Strouhal number	
T	Temperature	(K) (ºC)
x_0	Amplitude of oscillation	(mm)

Índex

i	Species i
*	State of supersaturation

List of acronyms

API's	Active pharmaceutical ingredients
OFC	Oscillatory flow crystallizer
OFR	Oscillatory flow reactor
HAp	Hydroxyapatite

FTIR	Transform-infrared spectroscopy
TEM	Transmission electron microscopy
ECSN	Embryo coagulation secondary nucleation

1. Introduction

1.1. Relevance and motivation

The crystallization/precipitation process plays a significant role in the pharmaceutical industry as it is the main purification process, of both intermediate compounds, and active pharmaceutical ingredients (API's) [1]. This technique is fundamental to achieve product quality, purity, and consistency, by controlling the crystal shape, size and polymorphic form that are of utmost importance in the pharmaceutical sector. Whilst offers high recovery and energy efficiency with a low environmental impact [1]–[3]. The precipitation (rapid crystallization) of hydroxyapatite has been widely studied due to its distinguished properties for medical applications, such as good osteoconductivity, biocompatibility, bioactivity and stability in the body fluids.

The quality of the mixture during crystallization plays a major role in controlling particle characteristics, especially the micro-mixture [4]. However, the crystallizers conventionally used in the industry are not capable of ensuring a uniform temperature and mixing control, because the crystallization process is mostly performed in batches [5]. The productivity and mixture control in this mode of operation can be highly problematic, leading to product variability from batch to batch, as well as difficulties in achieving consistent product specifications. This way, continuous crystallization has gained increasing attentions due to its advantages in terms of process controllability and productivity, overcoming many of the limitations associated with batch operations.[6]

The planar oscillatory flow crystallizer (planar-OFC) with smooth periodic constrictions is new geometry, within the oscillatory flow reactor technology (OFR), that offers several advantages to continuously perform crystallization/precipitation with high mixing control (at both micro and macro level).

The continuous synthesis of hydroxyapatite nanoparticles in a planar-OFC was already evaluated. In a previous work, [7] it was possible to produce nanoparticles with a mean particle size distribution of approximately 0.1 μm and a production rate of 23 g. h^{-1}. However, the particle size obtained did not remain constant over time. There was a limited timeframe in which the particle size was at the nanoscale, before the aggregation process took place and particle size shifted to the microscale.

In the context of pharmaceutical applications, it is crucial to obtain not only a narrow particle size distribution in the nanoscale, but also a particle suspensions stable over time.

That said, in this work, sodium citrate is used as surfactant agent to stabilise the nanoparticles dispersion and avoid the formation of aggregates during the continuous synthesis of HAp in a meso-OFR (planar-OFC).

1.1.Objectives

The challenge addressed to this work is the production of dispersed HAp nanoparticles in a meso-OFR (planar-OFC) with a precisely controlled particle size (<100nm) and a narrow size distribution, meeting the specific pharmaceutical requirements for drug delivery application.

The main objective of this work is to evaluate the effect of citrate to calcium ratio (Cit/Ca) on the dispersion/stability of HAp nanoparticles during their continuous synthesis in a meso oscillatory flow reactor, in order to obtain particles with the desired characteristics in the shortest amount of time.

It is also intended to increase the production rate by increasing the flow rate and the reactor dimensions. So, this study also aims to evaluate the continuous synthesis of HAp nanoparticles (with the same specific requirements) in a scale-up meso-OFR (planar-OFC) in the presence and absence of surfactant.

Thus, in addition to the main objectives, the following specific objectives can be identified:

- Minimizing the formation of intermediate calcium phosphate phases;
- Identifying the presence of citrate molecules in the surface of the obtained particles;
- Understanding the citrate mechanism applied to particle dispersion;

1.2. Thesis layout

The present work is organized in 7 different main chapters:

Chapter 1: Introduction, highlights the project's aims and objectives, as well as the organization.

Chapter 2: Context and state of the art, a theoretical introduction about the basic principles of the crystallization/precipitation process, and the oscillatory flow reactors technology. A summary of the main HAp characteristics and applications in the context

of pharmaceutical applications, as well as a highlight on the role of citrate in the HAp nanoparticles dispersion.

Chapter 3: Materials and methodologies, enumerates the materials used during the experimental work and the methodologies adopted, as well as the conditions of each operation.

Chapter 4: Results and discussion, contains the descriptions of the obtained results, their respective analysis and discussion considering the objectives and the literature.

Chapter 5: Conclusions, describes the main conclusions of the results obtained, limitations and future works.

Chapter 6: Bibliography, references used for the construction of the dissertation.

Chapter 7: Appendix, contains additional information of the work done in order to better understand some concepts discussed over the dissertation.

2. State of the art

2.1. Crystallization/Precipitation

Crystallization is a separation and purification technique in which a crystalline product is obtained [8]. In the context of the present study, the crystallization process may be defined as a phase change in which a substance or several substances are converted from the liquid state to a solid crystalline state, which is a solid with an ordered internal arrangement of molecules, ions, or atoms [9] There is no clear distinction between crystallization and precipitation processes. The term crystallization corresponds to a more general description while the term precipitation is commonly used to describe rapid crystallization, usually as a result of an irreversible chemical reaction. The particles formed during the precipitation process are typically less crystalline, exhibiting an amorphous phase [10]

2.1.1. Thermodynamics

A solution is a mixture of two or more species, typically classified as solute and solvent, that results in a single homogeneous phase. The solutions can be classified as unsaturated, saturated, or supersaturated based on the solute concentration. There is a maximum amount of solute that can be dissolved in a given amount of solvent under specific experimental conditions. When this maximum is reached, the solution is said to be saturated. This amount of solute required to obtain a saturated solution, under given conditions, is known as solubility or saturation concentration [11], [12]. When the solute concentration exceeds the solubility, the solution becomes supersaturated [1]. Supersaturation refers to a state in which the solution contains more solute than the one that can be dissolved under given conditions, being an essential requirement for crystallization to occur [13].

That being said, supersaturation is the fundamental driving force for crystallization to occur and can be expressed as the difference between the chemical potentials of a solute *i* in a supersaturated solution, μ_i, and in a saturated solution, μ_i^*, which are calculated by the equations (2.1) and (2.2).

$$\mu_i = \mu_i^0 + RT\ ln a_i = \mu_i^0 + RT ln(\gamma_i C_i) \tag{2.1}$$

$$\mu_i^* = \mu_i^0 + RT\ ln a_i^* = \mu_i^0 + RT ln(\gamma_i^* C_i^*) \tag{2.2}$$

Where R is the molar gas constant, T the temperature, C is the concentration in solution, α is the activity and γ is the activity coefficient. The index i refers to the species i and the * represents the state of saturation. Thus, the difference of chemical potentials is obtained by subtracting equations (2.1) and (2.2):

$$\frac{\mu_i - \mu_i^*}{RT} = ln\frac{a_i}{a_i^*} = ln\frac{\gamma_i C_i}{\gamma_i^* C_i^*} \tag{2.3}$$

In most cases, the activity coefficients are unknown, so, the difference of chemical potentials can be approximated by a difference of concentrations, ΔC, a ratio of concentrations, S, or the relative supersaturation, σ, according to the equations (2.4), (2.5) and (2.6), respectively:

$$\Delta C = C - C^* \tag{2.4}$$

$$S = \frac{C}{C^*} \tag{2.5}$$

$$\sigma = \frac{C - C^*}{C^*} \tag{2.6}$$

It is important to note that these definitions of supersaturation assume an ideal solution with an activity coefficient of 1 [12], [14].

2.1.2. Kinectics

2.1.2.1. Nucleation

The process by which solute molecules in a supersaturated solution combine to form a stable solid aggregate or cluster is known as nucleation. The spontaneous emergence of a new phase occurs only when the system is out of equilibrium.

Depending on the mechanism by which nucleation occurs, it can be classified as primary nucleation or secondary nucleation. Primary nucleation happens when the solution does not contain any crystalline matter [15]. Within this mechanism is possible to highlight two ways of occurring nucleation: homogenous nucleation, if the formation of nucleus occurs in a solution free of solid phase; or heterogeneous nucleation, if the formation of nucleus is triggered by the presence of foreign particles [16] Secondary nucleation refers to nucleation induced by pre-existing crystals from the species under consideration, in the solution [17].

<u>Homogeneous Nucleation</u>

In this type of nucleation, the formation of a solid phase occurs spontaneously from a supersaturated solution. There is not an accurate description for the nucleation process because the critical nucleus sizes are typically in the range of 100-1000 atoms, which difficult its study [18]. Many theories, more or less complex have been proposed to describe the nucleation process.

The classical nucleation theory is the most elementary and widely used theory for describing the spontaneous nucleation process. Molecules dissolved in a solution begin to aggregate due to local concentration fluctuations, resulting in the formation of a nuclei or clusters that can act as crystallization centres when a critical size is reached.

This process was thermodynamically descripted by Gibbs. The free energy change required for cluster formation, ΔG, is defined by the sum of the free energy change for the phase transformation, ΔGv, and the free energy change for the formation of the nuclei surface, ΔGs, as demonstrated in equation (2.7) [14].

$$\Delta \mathrm{G} = \Delta \mathrm{G}_v + \Delta \mathrm{G}_s = \alpha L^3 \Delta \mathrm{G}_v + \beta L^2 \sigma \tag{2.7}$$

Where σ is the surface tension and β and α are the form factors, based on the characteristic dimension L, of volume and area, respectively. Considering a spherical aggregate with radius r, $\beta=\pi$ and $\alpha=\frac{\pi}{6}$, the free energy change required for cluster formation can be written as:

$$\Delta \mathrm{G} = \frac{4}{3}\pi r^3 \Delta \mathrm{G}_v + 4\pi r^2 \sigma \tag{2.8}$$

The two terms of equation (2.7) have opposite contributions in the total free energy of the system as shown in Figure 1. The first term (ΔG_v), describes the supersaturated solution's spontaneous tendency to deposition and contributes to the reduction of the free energy of the system, since the solid state is more stable than the liquid. The introduction of a solid/liquid interface, on the other hand, increases the free energy proportionally to the surface area of the cluster. This way, the growth of clusters depends on the competition between a decrease in ΔGv, which favours growth, and an increase in ΔGs, which favours dissolution. Consequently, total free energy, ΔG, increases with cluster size until it reaches a critical size, r_c (Figure 1), after which it decreases continuously and growth becomes energetically favourable, resulting in the formation of crystal nuclei. Thermodynamics of a forming crystal must be considered as

size-dependent. That said, considering that the system always evolves towards the decrease of the total free energy, if a newly formed cluster has $r < r_c$, the cluster dissolves, if $r > r_c$, the cluster grows and if $r = r_c$, the cluster remains in the equilibrium with the solution. So, a nucleus can be defined as the minimum amount of a new phase capable of independent existence [18].

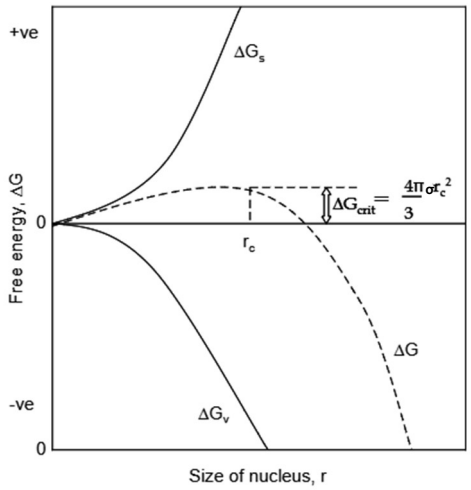

Figure 1- Free energy diagram for nucleation. Adapted from [79].

The critical radius is obtained by calculating the zero of the derivative of ΔG relative to r as demonstrated in equation (2.9):

$$\frac{\mathrm{d}(\Delta \mathrm{G})}{\mathrm{dr}} = 4\pi {r_c}^2 \Delta \mathrm{G}_v + 8\pi r_c \sigma \ = 0 \tag{2.9}$$

So that,

$$r_c = -\frac{2\sigma}{\Delta \mathrm{G}_v} \tag{2.10}$$

This way, the free energy change for the formation of a critical-size cluster, ΔG_c, is obtained by the conjugation of equation (2.8) and (2.10) [14].

$$\Delta \mathrm{G}_c = \frac{4\pi\sigma {r_c}^2}{3} \tag{2.11}$$

The velocity of nucleation, J, is given by the number of nuclei formed per unit time per unit volume and is expressed in the form of the Arrhenius reaction rate equation as:

$$J = A \exp(-\frac{\Delta \mathrm{G}_c}{KT}) \tag{2.12}$$

Where k is the Boltzmann's constant and A is the pre-exponential factor, related to the frequency of molecular collision in a solution.

The classical theory provides a simple and general framework to understanding and rationalizing the fundamentals of nucleation. However, several contemporary studies suggest that the nucleation process follows more complex pathways. For example, since this theory was developed for condensation of vapour to liquid, it does not provide any information about the structure of aggregates or pathways leading from the solution to solid crystal [18].

While the classical theory suggests a monomer addition model, where the cluster is formed by successive and organized attachment of single molecules, the two step nucleation model proposes the formation of a cluster of solute molecules in a first instance, followed by reorganization of that cluster into an ordered structure as presented in Figure 2 [18].

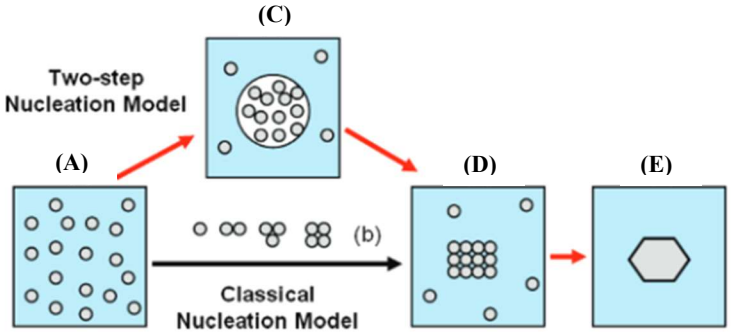

Figure 2 - Alternative pathways leading from solution to solid crystal: (A) supersaturated solution; (B) ordered subcritical cluster of solute molecules, proposed by classical nucleation theory; (C) liquid-like cluster of solute molecules, dense precursor proposed by two-step nucleation theory; (D) ordered crystalline nuclei; (E) solid crystal [18].

Heterogeneous Nucleation

In heterogeneous nucleation, the surface of foreign particles acts as a nucleation promoter by decreasing the free energy barrier for generation of the nuclei [19]. In fact, homogeneous nucleation is an unusual event, especially in large volume solutions (more than 100 L), where the presence of random contaminants, with surfaces that can act as nucleation promoters, are highly probable [20]. Practically is almost impossible to obtain a solution completely free of solid particles, so, heterogeneous nucleation is the most common mechanism in nucleation processes.

The r_c in the formation of nuclei remains the same for both homogeneous and heterogeneous nucleation; however, in heterogeneous nucleation, fewer molecules are required to produce nuclei with r_c. The free energy change in heterogeneous nucleation, $\Delta G'_c$, is smaller than the free energy change in homogeneous nucleation, ΔG_c, by the factor ϕ, as descripted in equation (2.13).

$$\Delta G'_c = \emptyset \, \Delta G_c \tag{2.13}$$

The factor ϕ is below 1, and only depends on the contact angle ($\cos\theta$) between surface of the foreign particle and the solute [14], [20].

$$\emptyset = \frac{(2 + \cos\theta)(1 - \cos\theta)^2}{4} \tag{2.14}$$

Which means that, when:

- $\theta = 180°, \cos\theta = -1, \emptyset = 1 \; and \; \Delta G'_c = \Delta G_c$
- $\theta = 0°, \cos\theta = 1, \emptyset = 0 \; and \; \Delta G'_c = 0$
- $0° < \theta < 180°, \emptyset < 1, \; \Delta G'_c < \Delta G_c$

These are the three main affinity possibilities between the solute and the surface of the foreign particles. The first case occurs when the solute doesn't have any affinity with the solid surface ($\theta = 180°$) and therefore the free energy change equals to the free energy change of homogenous nucleation. In the second case ($\theta = 0°$) the solute has total affinity with the surface and the free energy change is zero, which means the foreign particles are made of the same solute as the solution. At last, if the solute has a partial affinity with the surface of the solid ($0° < \theta < 180°$), the free energy change is less than the free energy change of homogeneous nucleation. As a result, nucleation is easier to achieve [14].

Secondary Nucleation

While primary nucleation usually prevails only at the initiation stage, when the solution is supersaturated, once crystals are formed and the supersaturation falls within the metastable zone, secondary nucleation becomes the primary mechanism of new nucleations [21]. Secondary nucleation can be explained by the interaction of the solution with existing crystals, the action of mechanical force and fluid shear stress, and the influence of supersaturation. Therefore, it can occur through several mechanisms, as demonstrated in Figure 3 [22].

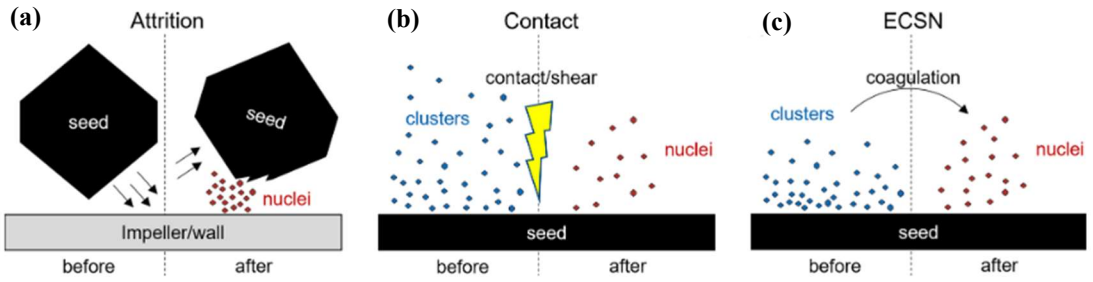

Figure 3- Illustration of three different mechanisms of secondary nucleation. (a) Secondary nucleation by attrition after collision with the impeller/wall. (b) Surface-induced secondary nucleation due to contact/shear. (c) Embryo coagulation secondary nucleation [22].

Secondary nucleation caused by attrition is a very common mechanism in industrial crystallizers. The collision of crystals (seed) with the impeller or with the reactor walls produces a large number of attrition fragments that can be considered as secondary nuclei. Depending on the degree of supersaturation, the fragments can grow or dissolve [21]. In contact nucleation, pre-formed clusters in the solution nucleate when they are close to other crystals already formed. It can occur simply as a result of contact with an external body, because of the fluid shear or due to an "autocatalytic" effect of the crystal surface. Embryo coagulation secondary nucleation (ECSN) is also a mechanism based on the effect of the crystal surface. However, in this case, van der Waals forces between clusters and crystals enhance the concentration of clusters nearby the crystal surface, which promotes the coagulation of clusters and generation of nuclei [22].

2.1.2.2. **Crystals Growth**

After nucleation, crystal growth takes place by the process of mass and heat transfer of molecules from the solution to the crystal surface. Once on the surface, the molecules are adsorbed and integrated into a suitable site on the crystal surface [23]. Figure 4 depicts a schematic representation of the atomic processes occurring during crystal growth. The surface of a crystal contains a flat region named terrace with raised partial layers, known as steps. Since the steps are not complete, they also contain sites called kinks. These are the three sites where a solute molecule can be integrated during crystal growth.

Kink sites are crucial in the process, since the molecules that attach there make more bonds with neighbouring molecules than the ones that attach to the terrace or to the

flat step edges. Besides being more energetically favourable, the incorporation at a kink site regenerates a new kink site for the next solute molecule incorporation [24], [25].

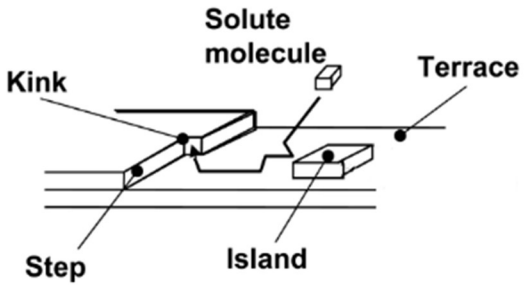

Figure 4- An illustration of the atomic processes on the crystal surface during crystal growth. Adapted from [24].

There are two main routes for crystal growth: Two-dimensional growth (Figure 5A) and spiral growth at screw-dislocations nucleation (Figure 5B). Two-dimensional growth is the most common path and consists of subsequent solute molecules incorporation at kink sites, where attractive forces are greatest, until the whole layer is completed. A monolayer island nucleus is always required as source of new steps and kink sites for the formation of a new layer. Since it is difficult to generate a nucleus island on a flat crystal surface, two-dimensional growth is only expected at relatively higher supersaturation levels. On the other hand, when the level of supersaturation is low, growth occurs essentially by spiral growth at screw-dislocations nucleation. In this model, a stress-induced defect in the crystal lattice acts as a solute molecule attractor, providing energetically favourable positions for further deposition, similar to kink sites in the two-dimensional growth model. In this route, crystals grow continuously since the system will always try to fit the imperfection, producing a continuous source of new steps [25], [26].

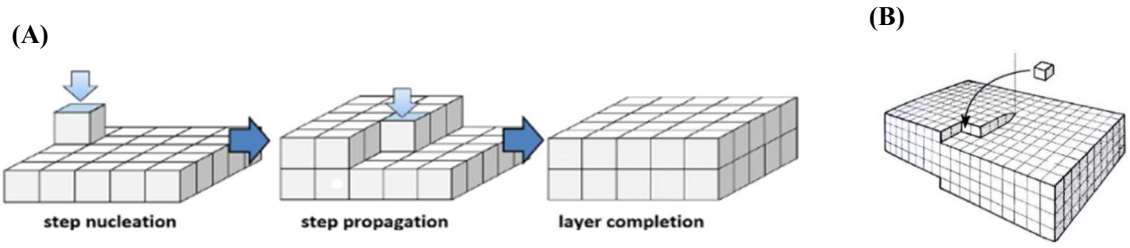

Figure 5- Illustration of two main routes for crystal growth: (A) Two-dimensional growth. Represented by a cascade of building block association events, where the blue block is the most recent associated one. (B) Spiral growth from a screw-dislocation [25], [26].

Even at the equilibrium, molecules are constantly attaching and detaching from the crystal surface. So, growth occurs when the flux of molecules attaching to the crystal surface exceeds the flux of molecules detaching from the surface. Reminding that, crystals grow while the solution is supersaturated, stop growing when it is just saturated, and are dissolved when it is undersaturated [4], [24].

Crystal growth rate, *G*, can be related with the degree of supersaturation by the following equation:

$$G = K_g \, \Delta C^g \tag{2.15}$$

Where g is the growth exponent and K_g the constant of crystal growth that can be expressed as a temperature dependence in the form of Arrhenius equation. As a result, the crystal growth rate can be written as:

$$G = A \times \exp\left(\frac{-E_a}{RT}\right) \Delta C^g \tag{2.16}$$

Where A is a pre-exponential factor and E_a is the activation energy of growth [14].

The crystal habit, or morphology, is determined by the different growth rates of each crystal face. Certain faces may grow faster than others, resulting in distinct shapes based on the dominant growth directions. For example, if the growth occurs uniformly in all three dimensions, the crystal become cubic. If it grows predominantly along one plane, the crystal will be plate-Like shaped. Or, if the crystal grows preferentially in one direction, it will assume a needle-like shape [25].

A variety of factors can influence and control the relative growth of a crystal's faces. Rapid crystallization, for example, may result in the formation of needle shape crystals [27]. The presence of impurities or additives (impurities intentionally added in the solution) may also have a significant impact on the growth rate of one or more preferred faces. Impurities/additives tend to adsorb on preferred growing faces, retarding and eventually stopping the growth of the new adjacent layers by blocking the crucial sites of crystal growth on those faces. This way, the use of additives is a useful tool to produce a desired morphological change in the crystal shape [25].

2.1.2.3. **Solubility-Supersolubility Diagram**

Figure 6 represents a diagram where the relation between supersaturation, spontaneous nucleation and crystal growth can be analysed by variations in temperature and concentration.

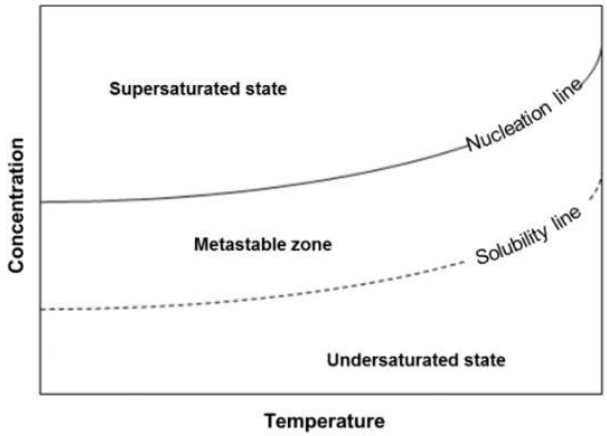

Figure 6- The solubility-supersolubility diagram [16].

The nucleation line and the solubility line define three distinct zones on the diagram: metastable zone, undersaturated state and supersaturated state. The equilibrium solubility of a solute as function of temperature is given by the solubility line. The region below that curve is undersaturated which means crystallization is not possible. It is a stable zone where existing crystals/nuclei are dissolved and disappear. The region between solubility line and nucleation line is called metastable zone. In this zone the solution is metastable which means crystals may grow, but spontaneous nucleation does not. In the absence of nuclei or crystal seeds, a supersaturated solution can remain indefinitely in this zone. Above the nucleation line, the solution is supersaturated and therefore spontaneous and rapid nucleation can occur [1], [9], [16], [28].

During crystallization/precipitation at a certain temperature, the solute concentration of a supersaturated solution decrease. The solute is instantly consumed by spontaneous nucleation until it reaches the metastable zone, where crystals can grow until the solute equilibrium solubility is achieved. After particle precipitation in a solution, the thermodynamics and kinetics of the suspension may oscillate due to secondary phenomena.

2.1.3. Secondary phenomena

Many phenomena can occur during and after crystallization which directly influence the characteristics (physical and chemical properties) of its final product, namely recrystallization, aging, agglomeration and Ostwald ripening.

Ostwald ripening is a phenomenon that occurs after crystallization, when crystals with different sizes remain on the saturated solution. Since the smaller particles have higher surface energy than larger ones and therefore higher solubility, the smaller crystals in the solution tend to dissolve and contribute for the larger crystals' growth [9], [29]

Agglomeration is a common phenomenon in crystallization mainly in industrial process when the production of crystals is high and so is the probability of particle interactions. It consists of the approximation and interaction between two or more particles to form a larger one. If the cluster of particles is just attached by weak cohesion forces (like van der waals), the phenomenon is named aggregation. On the other hand, if the particles stay in contact for a long period of time, a crystalline bridge can grow between them, and this phenomenon, in which particles are well cemented, is named agglomeration. This means that aggregation is a previous stage of agglomeration. However, while agglomeration is an irreversible process, aggregated particles can break-up and reaggregated by adding turbulent motion in the solution [30]

Aggregation/agglomeration can be undesirable since it can compromise the size and the purity of a crystal product [31], or it can be useful to manipulate the size distribution and the sedimentation of crystals, favouring the separation process [32]

2.1.4. Modes of Crystallization

To induce crystallization from a solution, a supersaturated state is required as a thermodynamic driving force**.** Several methods/techniques can be used to generate a supersaturated solution, namely solvent evaporation, cooling/warming, anti-solvent addition and chemical reaction.

In solvent evaporation method, the evaporation is reached by rising the solution temperature to its boiling point, which increases the solute concentration and leads to supersaturation. Cooling is the method where temperature dependence of solubility is used as a tool to achieve supersaturation. For example, if the solubility increases with temperature, the solution can be cooled bellow its saturation temperature, promoting the appearance of a solid phase. Anti-solvent addition is another technique where a compound is added to the solution to lower its solubility and therefore supersaturation becomes

easier to achieve. In the chemical reaction method, usually employed in precipitation, the crystallization can be directly achieved by adding two reactants solutions that produce low solubility products. The process occurs instantly, therefore the resulting product depends essentially on the reactants' mixture quality [9], [16], [28]

It is very important to select the appropriate method since different techniques for the same crystallization process can result in different yields and crystal properties (size, morphology, chemical purity, etc). The process's feasibility for the application in question and its industrial scale implementation is also crucial in the selection.

2.1.5. Critical crystals' attributes

Crystals/particles have several attributes such as size, yield, morphology, purity and size distribution that are critical for their characterization and often used as quality requirements/specifications [33] The size, distribution and morphology of the particles can affect bulk properties, product performance, processability, stability and appearance of the final product [34] So, they are critical parameters in the pharmaceutical industry for the evaluation of product consistency and quality. Size distribution is an important parameter in FDA process validation [35] A common approach to analyse the distribution width is to cite three values, d_{10} , d_{50} and d_{90} . The d_{50} value correspond to the median and is defined as the diameter where half of the population lies below. Similarly, 90 percent of the population lies below the d_{90} and 10 percent of the population lies below d_{10} [34]

2.1.6. Influence of mixing

Mixing influences the environment in which crystallization occurs and therefore the characteristics of the crystals. Since the growth rate and nucleation is highly dependent on the heat and mass transfers phenomena, the quality of mixing plays a large role in the process kinetics, affecting the characteristics of the final product, namely the particle shape, purity, size distribution and the degree of crystallinity [4]. This influence is increased in processes where the supersaturation state is very high, which is the case of the precipitation processes. At high supersaturated conditions both mixing time and reaction time are in the same order of magnitude [16]. Nucleation and crystal growth are directly influenced by the microenvironment, even more so than by the macroenvironment. This way, micromixing is essential to control mixing at the molecular level, mainly in crystallization by chemical reaction in which micromixing is crucial for the synthesis of a product with desired characteristics in terms of morphology, and size

distribution [4], [36]. For a better control of the crystallization/precipitation process and the quality of the products obtained, it is important to choose an equipment with a good mixing efficiency (at both micro and macro level), such as the oscillatory flow reactor.

2.1.7. Continuous Crystallization

The crystallization process in the chemical and pharmaceutical industries are mostly performed in batches due to tradition and regulatory issues. However, the scale-up, the productivity and the mixture control in this mode of operation can be highly problematic, leading to product variability from batch to batch, as well as difficulties in achieving consistent product specifications. In the past few years, continuous crystallization has gained increasing attentions due to its advantages in the process controllability and productivity. Continuous processes can overcome many of the limitations associated with batch operations. In comparison to batch crystallization, continuous crystallization requires a shorter development period to reach the industrial production, has lower facility costs and space requirements, causes fewer product quality fluctuations, and exhibits better process control.[6]. Depending on the reactor design, there might be no need for scale-up because even small scale systems may be able to produce large quantities given the unlimited operating time. In addition, higher productions can be easily achieved by increasing the number of continuous reactors (scale-out) [37]. According to Schaber et al.,[38] the continuous operation can reduce the production costs up to 40% of its value. Considering that the batch processes still dominates the industry due to the expertise and experience acquired regarding to the processes and equipment used. There is a great need to study and control the same processes in the continuous mode, so that they can also be easily implemented in the industry.

2.2. Oscillatory Flow reactor (OFR)

2.2.1. Description/mode of action

To perform continuous crystallization there are two main categories of crystallizers typically used: the mixed suspension mixed product removal (MSMPR) crystallizer and the plug flow (PF) crystallizer [39]. They differ from their mixing models, stirring mechanism and turbulent flow mechanism respectively [40]. In particular MSMPR crystallizers are often preferred because of their low cost and well stablished control and operation [41]. However they have several disadvantages, namely a highly localized shear region and non-uniform temperature and mixing control. PF crystallizers

are more interesting because they overcame the main challenges of continuous crystallization in MSMPR.

Recently, some other configurations have been developed based on PF technologies, altering its specific features, and increasing the potential for continuous crystallization [5], [42]. Among them is the oscillatory flow reactor (OFR), also known as oscillatory flow crystallizer (OFC) when applied to crystallization. This type of reactor consists of a tubular device containing periodically spaced constrictions, named baffles, whereby an oscillatory fluid motion transversely flows through [43]. The interaction of the fluid with the constrictions promotes the generation and expansion of eddies and vortices creating a strong radial motion that provides uniform mixing in each inter-constriction cavity and consequently along the entire reactor length, as shown in Figure 7 [5]. In other words, the zone between to constrictions is assumed to be uniformly mixed and act as a perfectly mixed stirred tank reactor.

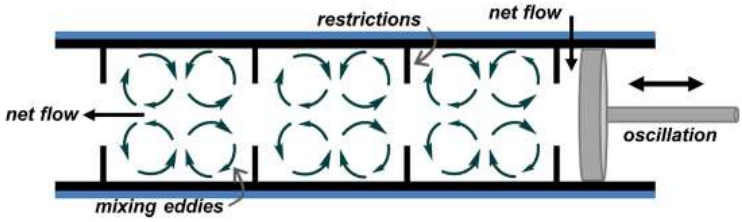

Figure 7 - Generation and expansion of vortices in a meso-OFR [5].

The vortices formation can be controlled through a combination of geometric and operational parameters, resulting in precise mixing control and efficient mass and heat transfer [44].

2.2.2. Geometric parameters: Planar-OFC

The OFR came as a promising technology to achieve crystallization because of its efficient mixing mechanism to enhance mass transport and to prevent solid deposition [42]. However, handling solids can be very challenging due to clogging issues, especially in small scales [45]. The solids tend to accumulate on the surfaces of the reactor, especially at low oscillation amplitude and frequency, leading to fouling and ultimately total reactor blockage [39], [46]

To overcome these and other limitations different baffles designs have been reported in literature, such as single orifice or multiple orifice baffles, helical ribbon and smooth periodic constrictions (SPC), amongst others [47]. Recently, a new geometry was created

by Ferreira et al., (2017). The new design is based on the OFR with SPC, where the typical circular cross-section was replaced by a rectangular cross-section, as shown in Figure 8. This new design is implemented as planar channels (planar-OFCs) in plate-like devices [39], [40], [48], [49]. Cruz et al., [40] have studied the mixing performance of a planar OFC and report that this new design exhibit better behaviour on solid suspension and transportation in comparison with the conventional OFR.

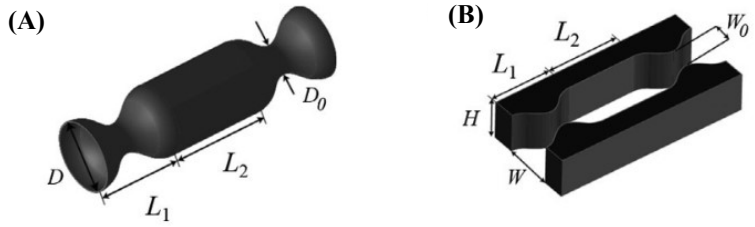

Figure 8 - Schematic representation of (A) a OFR with a circular cross-section (B) a OFR with a rectangular cross- section (planar-OFR). [48]

2.2.3. Operacional parameters

Literature shows that the mixing efficiency in a OFR is strongly affected by the frequency and amplitude of oscillation. Reis et al., [50] reported that frequency influences radial mixing, promoting the mixture in the spaces between two constrictions, while amplitude has an effect on axial dispersion. Later, Cruz et al., [39] confirms that planar-OFC has similar axial dispersion performance for both liquids and solids, which is of utmost relevance in the context of crystallization.

Oscillation conditions show a significant impact on the nucleation and crystal growth rate. Cruz et al., [51] report that the increase of mixing intensity in a planar-OFC by manipulating amplitude and frequency of oscillation lead to the formation of smaller particles with narrower size distributions. The same authors proved that crystal growth time decreases as both frequency and amplitude increase [52]. So, to obtain a large number of small crystals, high frequencies and high amplitudes should be combined. On the other hand, when a small number of large crystals are desired, low values of amplitude should be combined with intermediate to high values of frequency. However, it is documented that for low amplitude and high frequency condition, the vortices created after each constriction do not have time to expand through all the inter-constriction cavity due to the quick change of fluid direction. In these circumstances the mixing efficiency

of the reactor can be compromised due to a lack of mixing intensity which can create stagnant zones in the middle of each cavity [40].

The ratio of inertial forces to viscous forces in a flowing fluid as well as the mixing intensity and the effective vortex propagation in continuous operation can be expressed by three dimensionless groups: the Reynolds number, *Re*, the oscillatory Reynolds number, Re_o, and the Strouhal number, *St*, according to equations (2.17), (2.18) and (2.19) respectively [53].

$$Re = \frac{uD\rho}{\mu} \tag{2.17}$$

$$Re_o = \frac{2\pi f x_0 D\rho}{\mu} \tag{2.18}$$

$$St = \frac{D}{4\pi x_0} \tag{2.19}$$

Where u is the superficial net flow velocity, f is the frequency of oscillation, x_0 is the amplitude of oscillation, D is the internal tube diameter (in the straight section), ρ is the fluid density and μ the fluid viscosity. Together, the Re_o and the *St* characterize the overall mixing conditions in an OFR. So, In order to perform a linear scale-up in an OFR, the geometric and hydrodynamics similarities must be guaranteed, which is achieved by keeping dimensional groups constant [49].

The OFR can be operated in a vertical or horizontal position [40] in batch or continuous modes [5], [44]. Scale-Down is also a strategy often applied in OFR technology to promote the process intensification.

2.3.Process intensification /miniaturization

Process intensification (PI) is the most promising and growing field of research and industrial development in the chemical and biological process industries. Despite the significant growth of this subject over the past decades, there is no clear definition for PI [54]. The aim of the PI concept consists in adapting the process to obtain specific features such as: higher performances and yields; better product consistency and reproducibility; flexible production capacity; less usage of utilities and feedstock; energy and cost savings; easy scale up and scale down systems and safer processes [16], [55].

Different strategies can be used to achieve PI by acting on the equipment, in the method or in the plant design [54]. Miniaturization is a recent strategy used to intensify processes through the use of equipment. Miniaturization includes micro and meso-scale systems, where the major difference lies in the reactor dimensional structure. A micro reactor has microchannels under a millimetre in size, while a meso reactor has its channels sized between the millimetre up to a centimetre [16].

2.3.1. Meso-scale

Meso scale reactors have several advantages for research and industry applications. Their small footprint allows to save space, materials, and energy, while reducing capital and operational costs. When the dimension of a reactor decreases, the gradient of some physical variables such as pressure, concentration, temperature, and density increase, influencing heat and mass transfer and diffusional flux. For example, heat can be added and removed much more efficiently in a meso reactor than in a conventional macroscale reactor. So, the process control becomes easier. The response time is also shorter as well as the holdup volume. Other benefits are the efficiency of mixing and the possibility of continuous operation.

Since the reduction of size to a meso-scale decreases the production rate, a series of individual reactors should be combined to achieve higher production rates (scale-out) [56]. However, it is still possible to perform the scale-up within the meso scale.

2.4.Hidroxyapatite

2.4.1. Properties

Hydroxyapatite (HAp) is a calcium phosphate mineral from apatite family with chemical formula $Ca_{10}(PO_4)_6(OH)_2$. [57]. It has been widely used due to its similarity to the mineral component of mammalian bones and hard tissue. HAp is essential to biological and medical application due to its distinguished properties such as good osteoconductivity, biocompatibility, bioactivity and stability in the body fluids, which means that, when in contact with human body does not produce toxicity or inflammatory reactions. HAp is also able to provide a scaffold or template for new bone formation.

Stoichiometric HAp has a Ca/P molar ratio of 1.67 and it is the most stable calcium phosphate at room temperature and pH between 4 and 14 [58], [59] Nevertheless the chemical composition of a biological apatite differs from a synthetic stoichiometric HAp,

due to the presence of carbonates and essential trace elements (such as Na, Mg, Zn, etc) that causes structural imperfections in the apatite nanocrystals [60], [61]

The hexagonal form is the most common and stable structure of HAp, usually formed by precipitation at temperatures between 25 and 100ºC. The hexagonal HAp crystals also have an elongated shape because the growth occurs preferentially in one direction [61]. High temperatures may induce changes in the phase and structure of the HAp crystal, before or after its forms [62].

2.4.2. Pharmaceutical application

Recently, HAp is being used in the pharmaceutical industry allowing the drug delivery process to be more efficient and promising to solve several medical challenges [63]–[65]. Due to its properties, HAp crystals have emerged as a promising solution to treat infections by acting as carriers for genes, proteins and various drugs such as antibiotics, vaccines, steroids, hormones, analgesic, etc [66].

Conventional drug delivery systems have an instant and rapid drug release to both healthy and infected tissues, which can produce side effects. HAp nanoparticles presents huge prospects for controlled local drug delivery where the drug can be released for an extended period in the blood or at specific target tissues, limiting drug toxicity to adjacent organs [67], [68].

The influence of pH on the dissolution of HAp crystals can be advantageous for drug delivery. It has been noted that decreasing the pH on a solution from alkaline to acidic can increase the degradation rate of HAp. The tumours tissues environment has a typical pH value around 5, while the healthy tissues in human body have pH value of 7.4. This way, HAp has been studied for the potential to treat cancer, since its degradation is activated with the typical pH value of a tumour, releasing the drug at the target site [67], [69].

The chemical composition, crystallinity, size, surface and morphology of the HAp crystals and their aggregation play critical roles in determining their properties and potential applications. For example, nanoscale HAp particles exhibit better bioactivity and higher performance in drug delivery systems as compared with microscale particles[70]. However, producing nano-size particles can be very challenging, due to their high propensity to aggregate that reduces their stability in suspension. In addition, nanostructures with different morphologies show different performances. This way, the

desirable HAp nanostructure can be formulated to regulate the amount of drug absorbed and its release profile [67].

2.4.3. Processes for HAp precipitation.

A great variety of synthesis methods have been reported for the precipitation of nanostructured hydroxyapatite. Production of nanometric HAp can be broadly grouped into six sets of methods: dry, wet, hydrothermal, high temperature, synthesis based on biogenic sources and a combination of the aforementioned methods. But nevertheless only a few techniques are acceptable in terms of performance and economic consideration [65].

Dry methods are widely used for mass production of powders with no need for precise control, since they do not significantly influence the characteristics of the powders obtained. So, despite being a relatively simple and low-cost procedure, it is not appropriate for biomedical and pharmaceutical applications, in which precise control of product characteristics is extremely relevant [71]. Among all the methods, wet chemical precipitation is the most frequently used procedure because of its simplicity, low cost, and easy application in industrial production [72].

Different physicochemical characteristics can be achieved depending on the process parameters, like reaction temperature, reactant addition rate, Ca/P molar ratio, pH and stirring speed, etc [16], [73]. These conditions become decisive to determine the particle shape, size and nanostructure, and therefore they should be accurately controlled and stabilized to achieve the quality and reproducibility of the HAp synthesis [74]. In most of the HAp precipitation studies, higher crystallinity and purity are obtained by increasing the temperature and the pH respectively [32]. For example, Liu et al., 2001 reported that 1 day was needed to form pure HAp by adding equal parts of Ca(NO3) and (NH4)2HPO4 at 25°C, while, at 95°C only 5 min were required.

2.5. Hydroxyapatite synthesis in the presence of citrate ions

2.5.1. The role of citrate

Nanoparticles without surface modification may aggregate, due to polar and ionic surface forces [75]. Additives, such as polymers, surfactants or small molecules are commonly used in chemical synthesis methods to improve the colloidal stability and to control particle size and shape at the nanometer level [76]. Recently, the effect of sodium citrate on the growth of hydroxyapatite nanoparticles has received increasing attention

due to the detection of a large number of citrate (Cit) molecules strongly bound to the natural bone apatite surface [77]. Numerous studies have revealed that Cit can strongly control the dispersion, morphology and size of HAp nanoparticles during artificial synthesis, by an interaction between its carboxyl groups and the calcium ions (Ca^{2+}) [78]–[81].

Citrate stabilizes the HAp surface by inhibiting the crystal growth and thus promoting the synthesis of nanometric particles. However, citrate molecules tend to adsorb on preferred crystal faces, preventing the growth on those faces, which leads to the formation of needle or rod-like shape nanoparticles [82]. In addition, they bound to the interface of HAp generate a highly negative charged surface that prevents particle aggregation via electrostatic repulsion.

The influence of citrate to calcium molar ratio (Cit/Ca) on HAp synthesis has also been studied [83], [84]. Different morphologies and sizes can be obtained by varying the solution Cit/Ca molar ratio, as demonstrated in Figure 9.

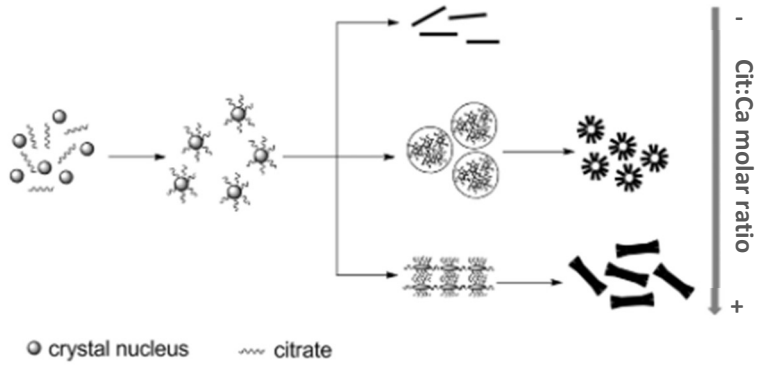

Figure 9 - Schematic Illustration of the Morphological Evolution of Hydroxyapatite Particles depending on the Cit/Ca molar ratio in solution [84].

Low Cit/Ca molar ratio tend to favour the synthesis of dispersed needle or rod-like shape nanoparticles. However, when the ratio increases, nanoparticles begin to aggregate in a spherical format, usually on the micrometric scale. If the Cit/Ca molar ratio continuous to increase, the morphology of the HAp structure changes to a sheetlike-structured particle. In summary, Cit/Ca molar ratio may affect the aggregation mode of nanoparticles influencing the structure of the final products [83], [84].

2.5.2. Mechanism of citrate adsorption at the atomic level

Citrate molecules have three carboxyl groups with pKa values of 3.1, 4.8, and 6.4, respectively. So, at pH>6.4 citrate is completely deprotonated as Cit^{3-} and can strongly

interact with Ca^{2+} on the HAp surface. Citrate molecules adsorb preferentially onto the precipitated particles surface, since they are too large to be incorporated into the crystal lattice [79]. The mechanism of interaction between the citrate and the HAp at the atomic level is still poorly understood. Many interaction models have been proposed to describe the interaction between the carboxylate groups and the calcium ion on the HAp surface, such as: a) One citrate binding two adjacent calcium ions, using two neighbouring carboxylate groups. b) Two carboxylates of one citrate interact with four calcium ions. c) Each carboxylate group interact with one calcium ion so that one citrate binds three calcium ions. The majority of these models were deduced from the Langmuir adsorption and computer simulation methods [85].

However, Jiang et al., [85] supported directly by an experimental measurement at the atomic scale, report that each calcium ion only binds to one side of the carboxylate group of one citrate molecule. Since only one carboxyl group bound to the HAp surface, the other two carboxylates of citrate are free and can interact with the remaining citrate molecules in the solution. The adsorption process of citrates onto the HAp surface undergoes two major stages, as illustrated in Figure 10.

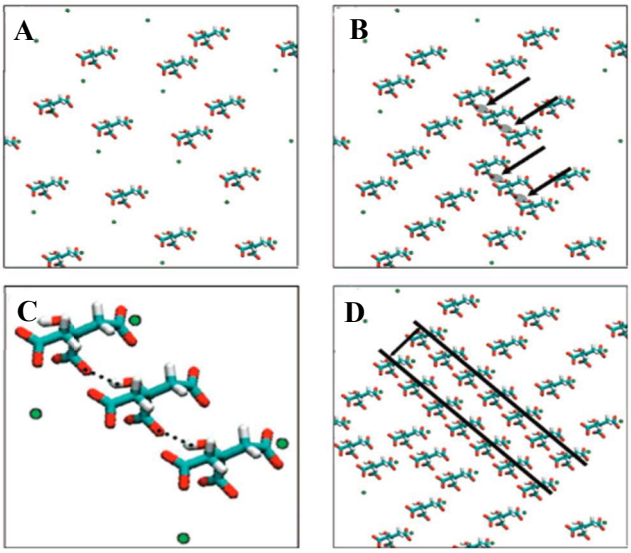

Figure 10 – Illustration of the self-assembly of the adsorbed citrates on the HAp. (A) Citrate molecules bond to the hap surface calcium ions at low citrate concentration. (B) Begin of the "side-by-side" citrate molecules assembly, along one direction, by the intermolecular hydrogen bonds (arrows), (C) Details of the hydrogen bonds between the neighbouring citrates and (D) Self-assembly of citrate molecules in the HAp surface, at high concentration.

At the initial stage, citrate prefers to bind to the calcium ions available on the surface of the HAp (by one carboxyl group interaction) (Figure 10 A). When all the calcium ions on the HAp surface have been occupied, the free carboxyl and hydroxyl groups of citrate tend to create intermolecular hydrogen bonds resulting on the linear self-assembly of citrate on the HAp surface (Figure 10 B-D). That being said, the Citrate adsorption on the HAp surface is mediated by two different kinds of interactions: a direct bond between citrate and the Ca^{2+}, and an indirect bound, from the linear self-assembly of citrate molecules in "inert" sites of the surface [85].

2.5.3. Role of HAp-Cit in drug delivery applications

Hydroxyapatite nanoparticles functionalized with citrate (HAp-Cit) are promising nanomaterials with high biomimetism, biocompatibility, and aqueous suspension stability, which have been used in a variety of medical applications, including drug delivery applications [86]. There is a growing interest in the development of nanomaterials with functionalized surfaces, with suitable functions for drug delivery applications. The surface modification can be an effective tool to manipulate molecule interactions and control the drug release according to environmental triggers such as pH and temperature. For example, Verma et al.,[87] report that the surface of HAp functionalized with citrate can significantly improve the loading efficiency of an anticancer drug (DOX, oxorubicin hydro-chloride), while exhibiting a pH dependent release that promotes drug releasing to specific cancer targets. Salahuddin et al., [88] also report the use of HAp-Cit nanocapsules to improve efficiency, load and delivery of an anticancer drug (aertesunate).

3. Technical description

3.1. Production of HAp nanocrystals/nanoparticles

3.1.1. Reactants preparation

The crystallization/precipitation occurs by chemical reaction with calcium chloride, $CaCl_2$, (Merck, 99.5%) and disodium hydrogen phosphate, Na_2HPO_4 (Sigma-Aldrich, 99.0%). Sodium citrate, $C_6H_5Na_3O_7 \cdot 2H_2O$ (Panreac, 99.0%), was used as source of citrate. The reactants were prepared with ultra-pure water (Milli Q water, resistivity of 18.2 MΩ.cm^{-1} at 25°C) with concentrations of 0.5 mol.mL^{-1} and 0.3 mol.L^{-1} for calcium chloride and disodium hydrogen phosphate, respectively. Sodium hydroxide, NaOH, (Pronolab, Portugal)) was added to the disodium hydrogen phosphate solution in a concentration of 0.41 mol.mL^{-1} to ensure a pH value between 9 and 13.

3.1.2. Experimental procedure

The experiments were performed in two oscillatory flow plate reactors (planar-OFR), operated horizontally. They differ mostly in terms of material and dimensions. The smallest reactor (Figure 11 A) comprises a volume of approximately 21 mL, with a rectangular cross section of 5×4 mm and consists of a plate-like crystallizer with three stacked plates: a polycarbonate plate at the top, and two Teflon plates, one at the middle and other at the bottom. On the other hand, the large reactor (Figure 11 B) comprises a volume of approximately 63 mL, with a rectangular cross section of 5×8 mm. This planar-OFR consists of a plate-like crystallizer with three stacked plates: two polycarbonate plates, one at the base and one at the top, and one aluminum plate coated with Halar® ECTFE in the middle.

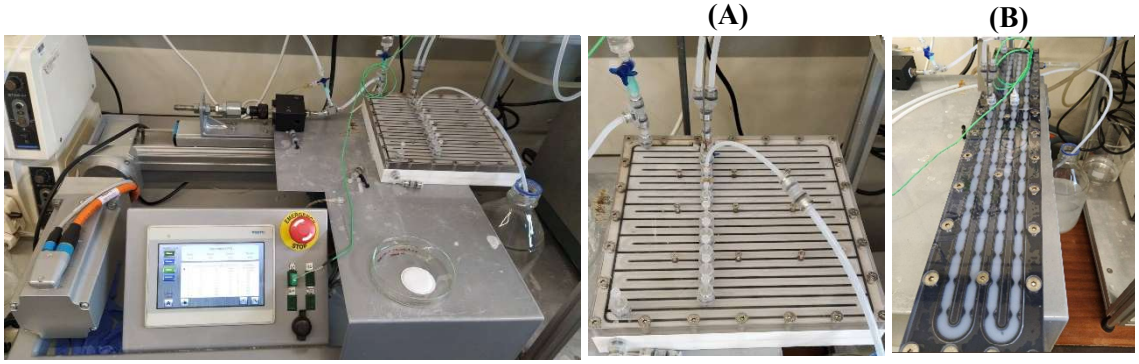

Figure 11- Experimental set up: (A) small reactor and (B) large reactor.

In the middle plate of both reactors, two channels were carved: one channel designed with a rectangular cross-section and smooth periodic constrictions at the top where the crystallization takes place; and one straight channel at the base where the water of a cooling/heating jacket circulates. The crystallization channel has 4 access points (one main inlet, one main outlet and 2 intermediate inlets/outlets).

The reactants were fed into the set-up by means of a peristaltic pump (BT300-2J, Longer Pump) previously calibrated with ultra-pure water. Figure 12 show the experimental set-up schematic representation. The $CaCl_2$ solution enters in the access point A. While the solutions of Na_2HPO_4 and $C_6H_5Na_3O_7$ (represented as B and C respectively) enter simultaneously through access point D, in order to minimize the formation of calcium citrate, $Ca_3(C_6H_5O_7)^2$, since the concentrations used were above its solubility limit. The suspension leaves the reactor at point F, which means crystallization process occurs between points D and F.

The oscillation was controlled by a linear motor actuating a piston with a 12.05 mm diameter (H01-23×166 / 80, LinMot). The temperature was not regulated (room temperature ~25ºC) but was monitorized by a sensor/probe (inoLab, WTW) at the access point E.

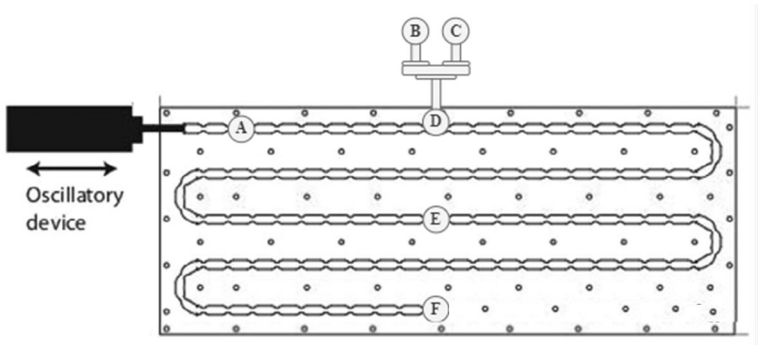

Figure 12- Experimental set-up schematic representation.

Before each assay, the reactor was filled with $CaCl_2$ without oscillation while a manual syringe was manipulated in the main inlet through a 3-way valvule. These procedures avoided the formation of bubbles and helps to drag them out.

The continuous crystallization/precipitation of HAp nanoparticles was performed under the same conditions of frequency of oscillation, *f*, (4Hz) for both the reactors, while the amplitude of oscillation, x_0, was 2.8 mm (90% of the cavity's volume) for the smallest reactor and 8.0 mm (~90% of the cavity's volume) for the larger one. These values were chosen considering preliminary tests.

Experiments on parameters such as surfactant concentration (Cit/Ca molar ratio) and flow rate were performed in two different sized reactors to assess the effect on particle aggregation. The respective information and operating conditions are presented in Table 1. The values of Cit/Ca molar ratio were chosen based on results reported in previous studies and preliminary tests. The flow rate was investigated with the goal of increasing the production [78], [81].

Table 1 - Description of the operating conditions tested for continuous crystallization/precipitation of HAp nanoparticles in two different meso-OFR sizes.

Reactor type	Q ($mL.min^{-1}$)	Cit/Ca
Small	68	0.0
	68	0.2
	68	1.6
	88	0.2
	88	1.6
Large	135	0.0
	135	0.2
	135	1.6

Each suspension was continuously collected after approximately three residence times, to ensure a stationary state, and the pH (MultiLab 540) was measured. The pH electrode was calibrated with two buffer solutions at pH=7.00 and pH=10.00 at 25 ºC. The liquid suspensions were then left to rest for further analysis, after a few days of maturation.

To obtain dry samples, 10 mL of each liquid sample were filtered (membrane of 0.2 µm pore size, Gelman Sciences, USA) and washed with a 50% (v/v) solution of ethanol and ultra-pure water and left to dry at T = 60 ºC. Then, the powder obtained was weighted for further yield estimative. Given the low temperature, it was assumed that the drying time do not significantly affect the mass.

After each assay, a sequence of ultra-pure water and acetic acid 5% (v/v) solution were fed into the set-up's access point A by means of a 3-way valvule and a peristaltic pump (ISMATECIPS 8, Switzerland) to clean the reactor/crystallizer.

3.2. Characterization of HAp nanocrystals/nanoparticles

The suspensions sampled at the outlet of the reactor were immediately analysed in the LS 230, Beckman Coulter, using water as solvent, to obtain particle size distribution in number and volume. This technology allows particle size analyses and particle characterization since it has the capacity for counting and sizing particles. The method detects particles with a diameter between 0,04 μm and 2000 μm assuming spherical particles to determine their diameter [89] The samples were reanalysed over the course of several days.

Powders were then characterized by Fourier transform infrared spectroscopy, FTIR (Bomem MB-154S). This technique was used to identify the sample composition since it is an effective analytical instrument for detecting functional groups and characterizing covalent bonding information by producing an infrared absorption spectrum.

The morphology of the particles was assessed by transmission electron microscopy (TEM) using an equipment (JEOL JEM-1400) located at i3S - Instituto de Investigação e Inovação em Saúde. This technique provides images of nanomaterials at a spatial resolution equal to the level of atomic dimensions. Beside spatial resolution in good quality and analytical measurements, TEM also allows information about the individual particle size, by image analysis [90]. The sample preparation for this technique consisted of the preparation of a suspension of 0.0200 g of dry sample in 0.5 mL of ethanol 70% (V/V). This suspension was then placed on a copper grid (StrataTek, Square Mesh Grids, 400 mesh, Copper) and analysed once completely dried. For a matter of time and economy only 6 samples were analysed.

As to the Ca/P molar ratio of the final product, total phosphorus was quantified by the ascorbic acid method (spectrophotometer PG Instruments Ltd. T60 UV/VIS) and calcium was measured by atomic absorption spectroscopy (spectrometer GBC 932Plus) at Escola Superior de Biotecnologia da Universidade Católica Portuguesa. Powders obtained were dissolved by the addition of a hydrochloric acid solution and resulting solutions were diluted to fulfil the detection limits of the equipment. For a matter of time and economy only 6 samples were analysed.

For the zeta potential measurements (Zetasizer nano series, Malvern Instruments), the liquid samples had to be diluted in a portion of 10 μl of sample to 1 ml of ultra-pure water, and then located in a clear disposable zeta cell. Evaluation of zeta potential is one of the most essential tests to validate the particles stability based on their electrophoretic

behaviour. The potential zeta is related with the tendency of particles to aggregate. When the value of the Zeta potential is farthest from zero, the higher is the charge on the particle surfaces and therefore the lower its tendency to aggregate

4. Results and Discussion

4.1. Continuous synthesis of HAp in the small reactor.

This study began by performing the synthesis of HAp by continuous precipitation in a reactor of smaller dimensions to ensure the continuity of a previous work [7]. Two Cit/Ca molar ratios and two different flow rates were tested (see Table 2) in order to achieve good suspension of the HAp nanoparticles and increase the production, respectively.

4.1.1. Final pH and production rate

The pH of the collected suspensions at the reactor exit was measured, as well as the mass of crystals obtained in 10 mL of solution after drying, to determine the production rate and yields. The results are listed in Table 2. The yield was calculated according (4.1).

$$Yield\ (\%) = \frac{m_{Hap,synthetised}}{m_{Hap,expected}} \times 100 \qquad (4.1)$$

Where $m_{Hap,synthetise}$ and $m_{Hap,expected}$ represents the mass of HAp obtained and expected respectively, in 10 mL of suspension. Considering that a stoichiometric HAp is formed (according to equation 4.2), in 10 mL of suspension it is expected to obtain 0.25 g de HAp.

$$10\ CaCl_{2\,(aq)} + 6\ Na_2HPO_4 \rightarrow\ Ca_{10}(PO_4)_6(OH)_2 \qquad (4.2)$$

Table 2 - Final pH value, crystals production rate ($g.h^{-1}$) and yield for each studied condition of flow rate, Q ($mL.min^{-1}$) and Cit/Ca molar ratio.

Q ($mL.min^{-1}$)	Cit/Ca molar ratio	pH	$m_{Hap,synthetised}$ (g)	Yield (%)	Production Rate ($g.h^{-1}$)
68	**0**	12.5	0.217	86.9	88.7
	0.2	12.5	0.140	55.9	57.0
	1.6	12.3	0.118	47.0	48.0
88	**0.2**	12.5	0.111	44.3	58.4
	1.6	12.3	0.129	51.6	68.1

Precipitation of calcium phosphates is highly influenced by the pH value of the solution [91]. The calcium phosphates phase formation, at 25°C, can be understood in terms of a typical solubility phase diagram, in which solubility isotherms are expressed as plots of log[Ca] and log[p] as a function of pH (Figure 13 A). Figure 13 B shows the phase diagram as a two-dimensional graph, for an easier examination. For a given pH value, any salt whose isotherm lies below another, will be less soluble (more stable) than the other salts [16], [92]. The diagram shows that the HAp is the least soluble phase for a pH> 4.5. High pH values need to be ensured to favour the presence of PO_4^{3-} ions in solution, which is essential for the formation of HAp phase. Increasing the pH to values higher than 12 favours the formation of HAp from a thermodynamic perspective (Figure 13).

In the present study, the pH values obtained after crystallization were above 12, for all the conditions evaluated (Table 2), which means that a pH value has been guaranteed to favours the formation of HAp instead of other calcium phosphates..

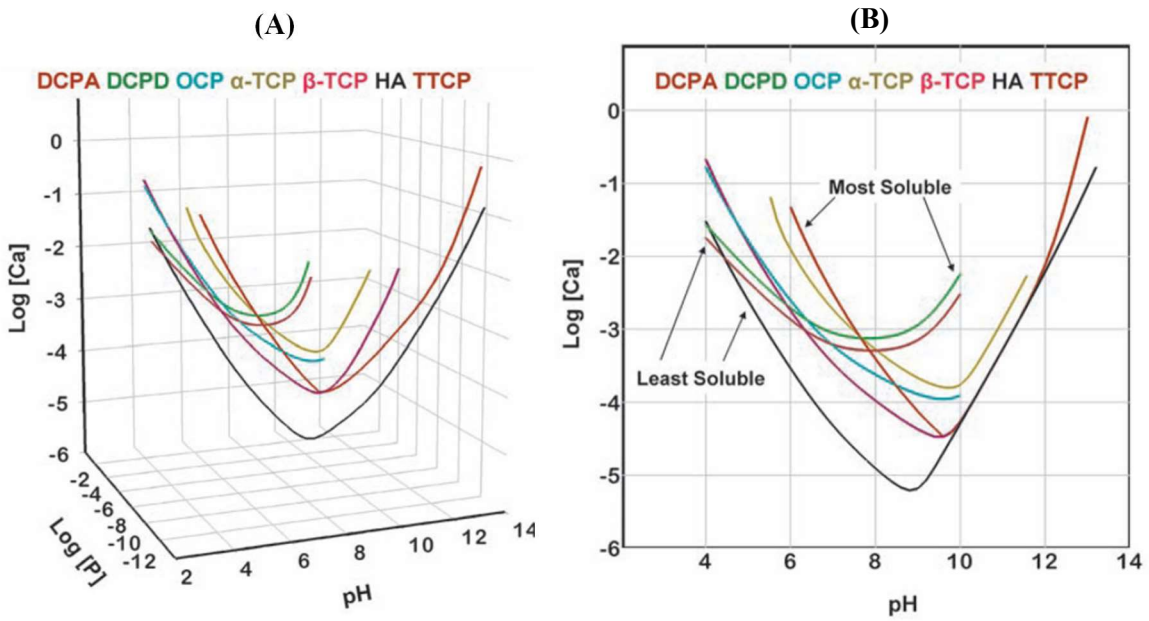

Figure 13- Solubility isotherms of calcium phosphates at 25°C. (A) Three-dimensional view and (B) two-dimensional view [92].

In the presence of Citrate, the yields were very low, about 50% (Table 2), which was also reflected in the production rate. Considering the volume, the concentration of the reactants and the stoichiometry of the reaction (see equation 4.2), a HAp production rate of 102 and 132 g. h^{-1} would be expected for the flow rate of 68 and 88 mL.min^{-1} respectively. However, it was observed that the filtrate was not fully transparent. The

particle matter may have escaped through the filter pore (2µm) or through its side, because smaller particles were produced in the presence of citrate (as reported in the section 4.1.5). Considering this observation and the yield close to 90% in the condition without citrate, it is believed that the production rate obtained in the presence of citrate is not representative of its real value. However further studies would be needed, using a smaller pore size filter to confirm the results. Furthermore, these yield calculations may be incorrect since the formation of a stoichiometric HAp was considered, which according to the Ca/P results described in Section 4.1.2.2 did not occur.

4.1.2. Phase identification

The composition of the precipitate obtained was evaluated by the functional group analysis, using Fourier-transform infrared spectroscopy (FTIR), and the calcium to phosphorus (Ca/P) molar ratio determination.

4.1.2.1.**Functional group analysis**

The FTIR analysis aims to provide information on the identification of the precipitate phase as well as the presence of adsorbed citrate species on the formed particles. The spectra of the studied conditions are presented in Figure 14, as well as the spectrum of a commercial HAp as reference.

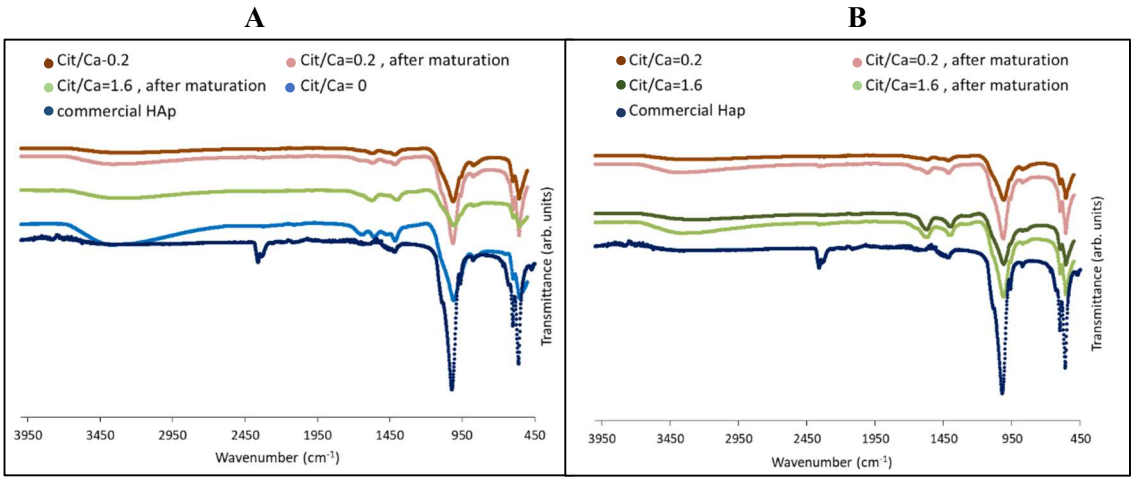

Figure 14- FTIR results corresponding to HAp particles synthesized with different Cit/Ca ratios and flow rates: (A) 68 mL.min^{-1} and (B) 88 mL.min^{-1}, and a comparison with a commercial Hap spectrum (900203, Sigma Aldrich).

The spectrum of the sample produced without citrate (Figure 14 A) is similar to the spectrum of a commercial HAp, as expected considering a previous work [7]. It only differs by the presence of the absorbed water band between 2500 and 3500 cm^{-1} and the

presence of carbonates. Generally, the intensity of the peaks is higher after a few days of maturation, which may point to an increase in crystallinity. A random spectrum from the samples produced with citrate (Q=68 mL.min^{-1} and Cit/Ca=1.6 after maturation) was selected and represented in Figure 15, for detailed functional group analysis. The functional group peak positions obtained for each spectrum were also summarized in the table A1.1 from the Appendix 1.

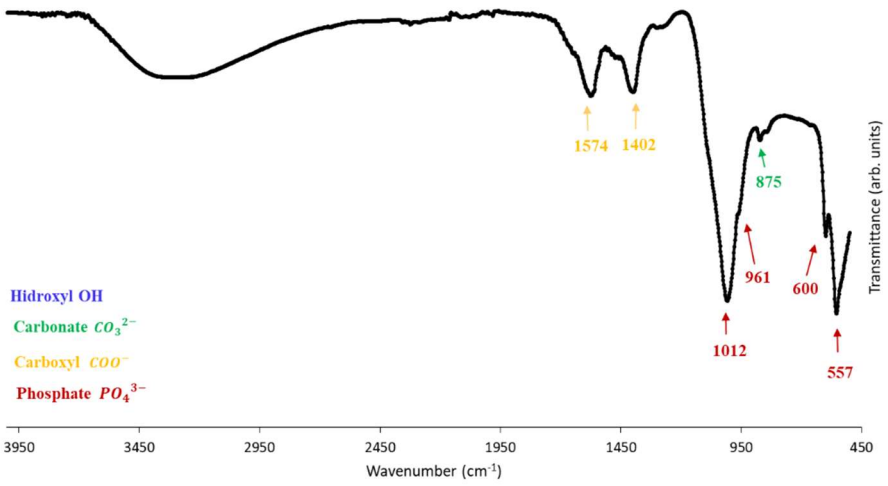

Figure 15 - FTIR spectrum for the condition of Cit/Ca=1.6, after maturation and Q=68 mL.min^{-1} with different functional group peaks identification.

It was possible to identify the peaks of three phosphate vibrational modes, v_1, v_3 and v_4, assigned to the HAp phase. The intense and well defined peak observed at 1012 cm^{-1} can be assigned to the phosphate group (v_3 vibrational mode) as well as the peaks on the position 600 and 557 cm^{-1} (v_4 vibrational mode) and 961 cm^{-1} (v_1 vibrational mode). The v2 vibrational mode, usually localized at 472 cm^{-1}, was outside the spectral region analysed [93].

The most characteristic peak of hydroxyapatite is located at 3570 cm^{-1} and is related to the hydroxyl stretch. However, in that spectral region (between 2500 and 3700 cm^{-1}) of Figure 15, it is possible to detect a broad band/peak that may be masking the hydroxyl peak. This band is attributed to the presence of water in the HAp powder, as reported before [94]. Which, in the context of this work, can be explained by the low drying temperature (60 ºC) applied in the methodology, to avoid phase transformations caused by higher temperatures.

Is highly common to find carbonate ions, CO_3^{2-} , in synthetic hydroxyapatite, due to the possible dissolution of CO_2 during reactants preparation [95]. Its integration in the

HAp crystal lattice can occur by phosphate ions substitution (B-type carbonate doping, associated to v_1 and v_3 vibrational modes) or by hydroxyl ions substitution (A-type carbonate doping, associated to v_2 vibrational mode) [86]. In the spectra of HAp produced without citrate, the presence of carbonate ions was confirmed by the identification of all the three peaks of v_3 vibrational mode. (Table A1.1 from Appendix 1). However, in the samples produced with citrate it was only possible to identify the vibrational mode associated with the A-type carbonate doping, at the position 875 cm-1, as pointed in Figure 15. The absence of B-type carbonate doping may be explained, because both carbonate ions and citrate molecules enter into crystal lattice as phosphate substituents [96], [97]. So, a competition may have occurred between the carbonate and citrate ions for binding to the calcium ion from HAp. Reminding that those vibrational modes can also be masked by the citrate related peaks.

These results suggest that citrate had no significant influence in the formation of the apatite phase, since the main functional groups of the HAp were identified in the obtained spectra. Still, it was possible to identify peaks related to citrate adsorption on the HAp surface. The peaks at 1574 and 1402 cm^{-1} are attributed to the antisymmetric , v_{as}, (1542- 1602 cm^{-1}) and to the symmetric, v_s , (1342-1409 cm^{-1}) stretching modes of carboxyl groups from citrate coordinated to HAp surface Ca^{2+} cations [76]. For an easier analysis of the citrate related peaks, a magnification of the FTIR spectra, in the range of 2000-1250 cm^{-1}, is presented in the Figure 16.

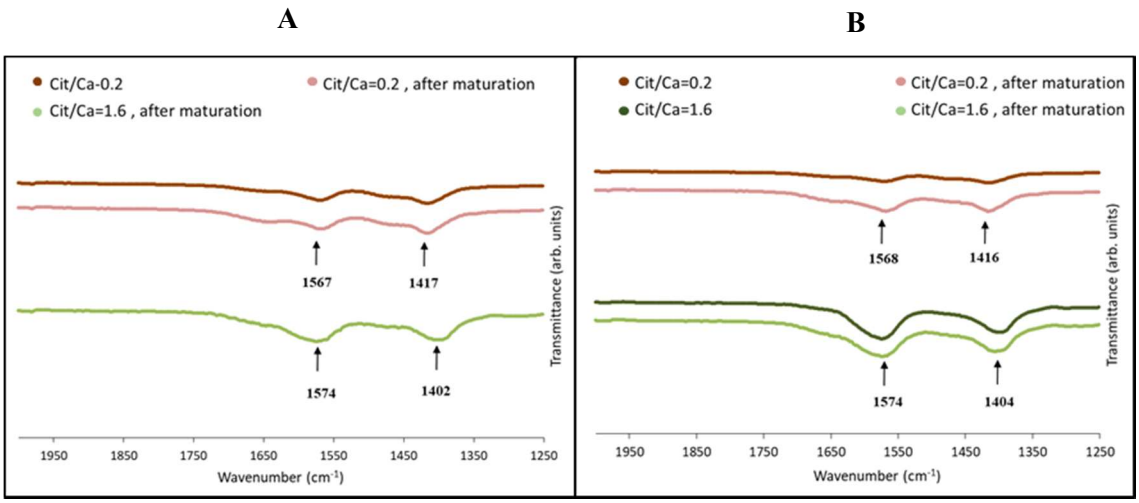

Figure 16 - FTIR results corresponding to Hap particles synthesized with different Cit/Ca molar ratios and flow rates: (A) 68 $mL.min^{-1}$ and (B) 88 $mL.min^{-1}$. Magnification of the 2000-1250 cm^{-1} spectral region.

The results indicate that the intensity and position of carboxyl related peaks change when a higher concentration of citrate is used. Peak intensity increases with the increase of Cit/Ca, which is expectable, given the increased concentration of citrate and the consequent availability of carboxyl groups [81]. Regardless of the flow rate, it is possible to detect a slight difference in the two peak positions obtained from Cit/Ca=0.2 and from Cit/Ca=1.6, as highlighted in the Figure 16. This shift in the peak position may be related to the type of interaction between the carboxyl group from citrate and the calcium ion from HAp (see the main type of interaction in Figure 17).

The variation between the symmetric and antisymmetric ($\Delta\nu$) peaks was calculated for all the conditions and is presented in table A1.1 from the Appendix 1. Considering these values and the information in the Figure 15, on the characteristic peaks for each type of interaction, it was possible to determine that the increase in citrate concentration (from Cit/Ca=.02 to 1.6) led to the change of the interaction mode: from an ionic to a pseudo-bridging interaction [76].

In summary, the results confirm that regardless of surfactant addition (sodium citrate), the phase of the particles produced in this reactor was HAp. Nonetheless, it seems that in the presence of surfactant, a less carbonate HAp was produced. The increase in surfactant concentration also allowed for the identification of changes in the mode of interaction of the citrate with the surface of the particles, at the atomic level.

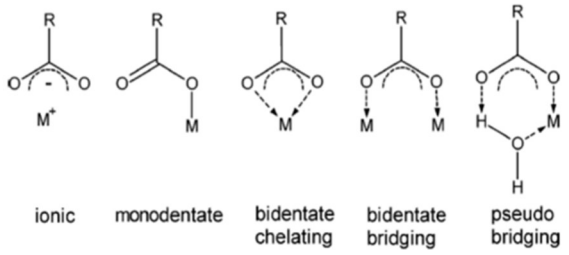

Type of interaction	Wavenumber shifts (cm^{-1}) ν_{as} COO^-	$\nu_s COO^-$	$\Delta=\nu_{as}$ COO^--$\nu_s COO^-$
ionic	~1560	~1409	~151
monodentate	~1602	~1342	~260
bidentate	~1542	~1440	~102
bidentate bridging	~1556	~1393	~163
pseudobridging	~1588	~1391	~197

Figure 17- Main types of interaction between a carboxylate ligand and a cation, and the respective peak positions for the carboxyle stretching. Adapted from [76].

4.1.2.2. **Ca/P molar ratio**

The mass fraction of the calcium and phosphorus elements of the precipitate was also quantified. The Ca/P molar ratio was then calculated and is listed in Table 3, for five conditions. The goal of this analysis was to confirm the formation of HAp in the precipitate obtained.

Table 3- Ca/P molar ratio of HAp synthesized in five different conditions of Cit/Ca molar ratio and flow rate. Comparison with the regulated values for European Union (ISSO 13779:2000) and United States (ASTM F1158-88:1993). *Ca/P molar ratio obtained from a previous study, in the same equipment and conditions of oscillation [7].

Q (mL.min^{-1})	Cit/Ca molar ratio	Maturation	Ca/P molar ratio
68	0	-	1.15
	0.2	No	1.27
	0.2	Yes	1.41
	1.6	No	1.49
	1.6	Yes	1.31
15	0	-	1.65*
ISSO 13779:2000 ASTM F1158-88:1993			$1.65 \geq Ca/P \leq 1.82$

One of the goals of this study was to obtain HAp instead of other calcium phosphates, therefore a molar ratio Ca/P of 1.67 was expected, corresponding to a stoichiometric HAp.

In a previous work [7] HAp nanoparticles were produced with a ratio of Ca/P=1.65, operating with a flow rate of 15ml.min^{-1} (Table 3). To increase the production rate, in the present study, the production of HAp was performed with a flow rate of 68 mL.min^{-1}, while maintaining the same reactor type and oscillation conditions (frequency=4Hz and amplitude=90% Cell volume). Considering this information, it would be expected a Ca/P molar ratio near to 1.65 and within the regulated interval, at least in the condition without citrate. However, the results in table 3 reveal that it was not possible to produce the desirable apatite phase, since all of the Ca/P molar ratios were below 1.65. These values are not compliant to the regulated production intervals of HAp set by the European Union and the United States of America.

A ratio of Ca/P=1.15 was obtained for the condition of Q=68 mL.min-1 and Cit/Ca=0. The Ca/P molar ratios close to one are characteristics of phases such as monenite (dicalcium phosphate) and brushite (dicalcium phosphate dihydrate), known as precursors of HAp formation [92]. The increase in flow rate from 15 to 68 mL.min^{-1} led to a decrease in the residence time from 1 minute to 13 seconds, which may be the cause for the low Ca/P ratio obtained. Despite a pH value has been guaranteed in which the monitite and brushite phases are more soluble than HAp (see Figure 13), the residence time in the

reactor may not have been sufficient hight for the transformation of these intermediate phases into HAp. The results from this analysis were the last to be obtained, therefore, there was no time to repeat the tests maintaining the residence time of the previous work. Yet, further studies should be conducted to assess the effect of residence time on the apatite phase formation.

The results of table 3 also show an increase in the Ca/P ratio as the citrate ratio increases (without maturation). This relationship was expected and can be explained by the competition/substitution between the phosphate and the citrate ions to bind the Ca^{2+} on the HAp nanoparticles surface. Regarding the maturation time, the results do not allow to draw conclusions since they were inconsistent between Cit/Ca ratios.

In Summary, these results suggest the formation of other calcium fosfates insted of HAp. However, this observation seems to be related to the residence time rather than the presence of citrate molecules. As a result, it is still relevant to investigate the effect of citrate as a surfactant agent in the synthesis of HAp nanoparticles. Nevertheless, this study should be repeated in a system that favours the production of HAp to confirm that the increase of Ca/P caused by the presence of citrate does not exceed the regulated values of the production of HAp.

4.1.3. Effect of citrate on particle size distributions

Analysis of the suspensions by laser diffraction (LS 230 by Beckman Coulter) provided information about the particle size distribution. In a previous work [7] it was possible to produce nanoparticles with a mean size distribution of approximately 0.1 μm. However, it was observed that the particle size did not remain constant over time. There was a limited timeframe in which the particle size was at the nanoscale, before the aggregation process took place and particle size shifted to the microscale. In this work, different concentrations of citrate were evaluated with the aim of obtaining dispersed nanoparticles and stable particle size distributions over time. The particle size distributions, in number, for the calcium phosphates (CaP) produced in the absence and in the presence of citrate is presented in Figure 18 and Figure 19, respectively.

Starting from the oscillatory conditions (frequency=4 Hz and amplitude=90% of the cavity's volume) of the previous work, the flow rate was increased from 15 $ml.min^{-1}$ to 68 $mL.min^{-1}$ in order to increase the production (Figure 18). With the flow rate of 68 $mL.min^{-1}$ it was no longer possible to observe particles at the nanoscale, the initial particle

size distribution was shifted to the micro scale and remained approximately constant over time. Which means higher flow rates (with higher energy) may improve the mixing in the reactor channels, increasing particle interaction and so their tendency to aggregate.

The results in Figure 19 suggest that the influence of citrate on HAp synthesis is not immediately apparent, since the particles remain aggregated at the end of the reactor (0 days). There is a required maturation timeframe for the citrate molecules to be adsorbed onto the HAp surface. As a result, variations in the particle size distributions were noticed over time.

The ratio of Cit/Ca=0.2 (Figure 19 A and C) was found to be an insufficient amount of citrate for an effective particle dispersion. The particle size distributions were unstable throughout time, fluctuating between the micro and the nanoscale. It is important to note that the distributions highlighted with the triangular marker correspond to the average of three non-conforming measurements (see example in the Appendix 2). The suspensions do not consist of a mixture of primary particles and aggregates. In fact with this amount of citrate the particle size distribution is extremely sensitive to changes in the state of rest. Correia, [78], have already reported this instability for a low Cit/Ca ratio. It is also possible that this state of instability is transitory, and that it takes more than 30 days for the ratio of Cit/Ca=0.2 to be able to disperse the particles so that nanoscale distributions can be obtained.

On the other side, at a flow rate of 68 $mL.min^{-1}$, the ratio of Cit/Ca=1.6 (Figure 19 B) allowed to obtain particles at the nanoscale, after only one day of maturation. These results remain constant over the period of 30 days which confirms the potential of citrate as a powerful tool to disperse the HAp nanoparticles, as expected in the objectives of this work.

With a flow rate of 88 $mL.min^{-1}$, tested with the aim of increasing the production, the ratio of Cit/Ca=1.6 (Figure 19 D) also allowed to obtain particles at nanoscale. However, a longer maturation period (2 days) was required in comparison to the flow rate of 68 $mL.min^{-1}$. This could be related to the propensity for particle aggregation, when a higher flow rate is being used, as already discussed.

In general, the ratio of Cit/Ca=1.6 demonstrated to be the most efficient condition for particle dispersion, given the ability to obtain particle size distributions in the nanometric range, in the shortest amount of time. However, an intermediate Cit/Ca ratio should also

be tested to assess whether the same effect may be obtained with less citrate concentration, hence minimizing contaminations.

Correia, [78] conducted a study similar to the current one but in a NETmix® reactor, and reported that 4 days of maturation, with the highest citrate ratio (not specified), was required to obtain particle size distributions in the nanometric range. In comparison, in the present study, nanoparticles were successfully obtained just after 1 day of maturation using higher reactant concentrations.

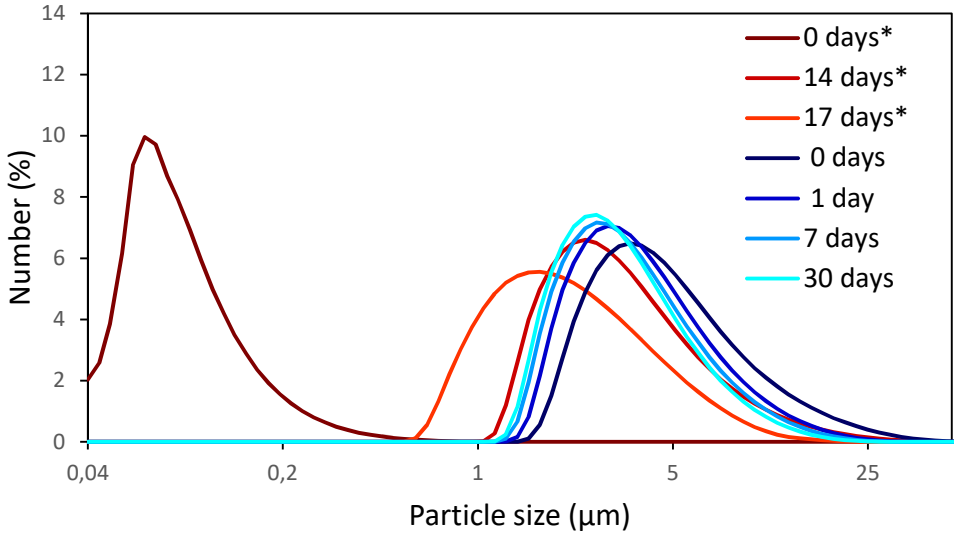

Figure 18 - Particle size distribution, in number, of the particles synthesized without citrate, at different maturation times. The * represent values obtained in a previous work for the HAp particles [7].

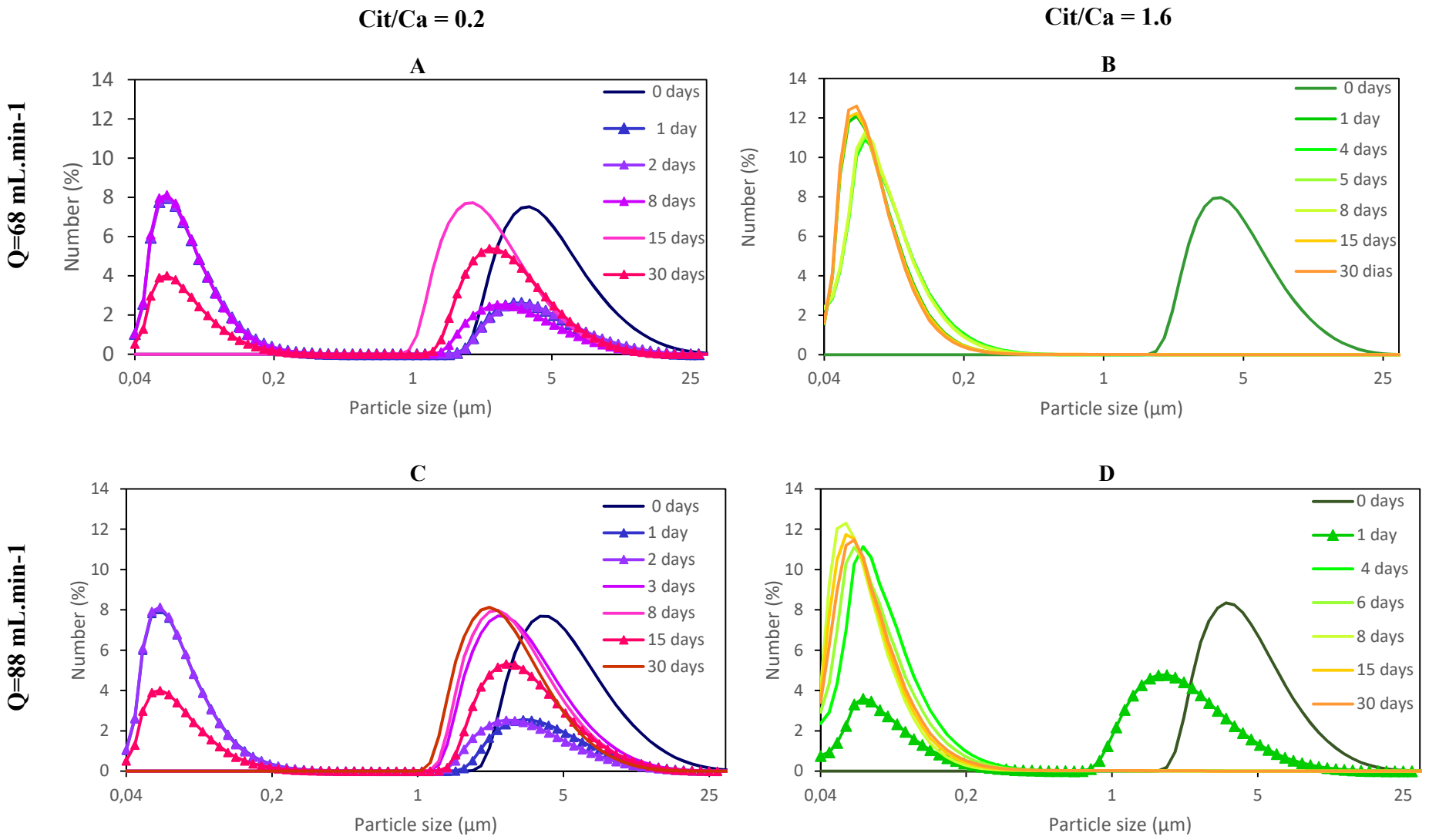

Figure 19 - Particle size distribution, in number, obtained after different maturation times, of the particles synthesized with different Cit/Ca ratios and flow rates. (A) Q=68 mL.min^{-1} , Cit/Ca=0.2 (B) Q=68 mL.min^{-1} , Cit/Ca=1.6 (C) Q=88 mL.min^{-1} , Cit/Ca=0.2 and (D) Q=88 mL.min^{-1} , Cit/Ca=1.6.

4.1.4. Effect of citrate on suspension stability (Zeta Potential)

The particles stability in solution was evaluated by measuring the zeta potential. In this technique, the electrophoretic behaviour of the suspended particles was studied to evaluate their propensity to interact and aggregate [76]. Figure 20 show the zeta potential evolution with the increase of Cit/Ca for the two different flow rates studied.

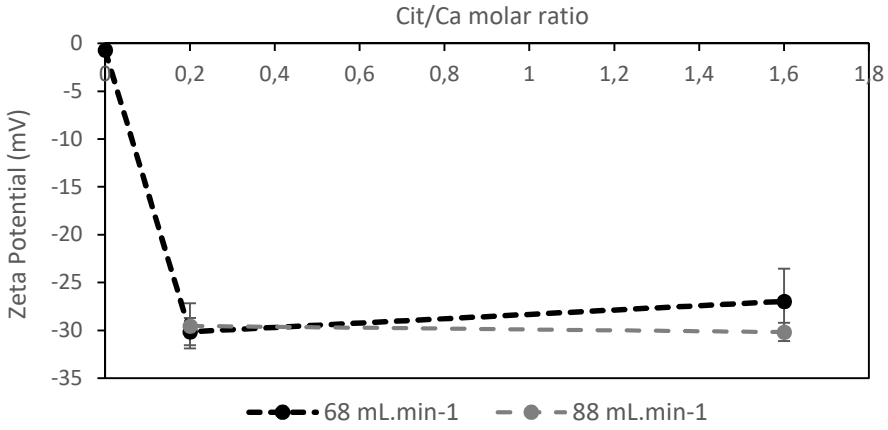

Figure 20- Zeta potentials of the particles produced with different Cit/Ca ratios.

In the absence of citrate (Cit/Ca=0) the formed particles exhibit a zeta potential value (ξ) very close to zero, which means they have a neutral surface charge and therefore a very high propensity to aggregate, as expected given the size distributions results previously discussed (see Figure 18).

The sodium citrate is used to achieve the particles dispersion by acting on their surface charge. The more distant from zero is the zeta potential, the strongest are the electrostatic repulsion between particles and consequently the better is their dispersion in the solution. In the presence of citrate, the zeta potential was found to be around -30 mV (Figure 20), which confirms the effect of citrate on the calcium phosphate particles surface stabilization. The carboxylate ions from citrate molecules are responsible for the negative charge on the surface of the calcium phosphate nanoparticles, promoting their electrostatic repulsions. These results are in line with those reported by Xiaoying et al.,[81]. Zeta potential values between ±30 and ±40 mV are indicative of moderate electrostatic stability. Nevertheless, the results in the Figure 19 show that the zeta potentials do not increase with the increase of citrate concentration.

Considering that the value of zeta potential remains constant for both the Cit/Ca ratios (0.2 and 1.6), the ratio of Cit/Ca=0.2 should be a sufficient amount of citrate to cause the particle dispersion. However, as previously observed, the particle size distributions for

that citrate ratio still revealed the presence of aggregates. The size and the aggregation state of the nanoparticles are two factors with high influence in the zeta potential measurements and interpretation. Pochapski et al., [98] reported that, at the nanoscale, the same value of zeta potential maybe obtained for two distinct samples even if they have particle with different sizes and aggregation states. When the suspension contains aggregates, high zeta potential values may be erroneously obtained which do not necessarily reflect high colloidal stability.

4.1.5. Effect of citrate on particle size and Morphology

TEM analysis was performed to evaluate the influence of citrate molecules on the individualized particle size and morphology. Figure 21 shows some of the images obtained.

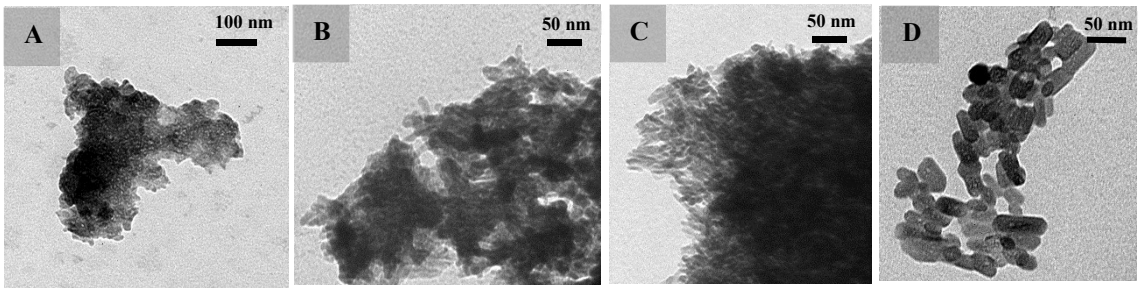

Figure 21 - TEM images of Hap nanoparticles obtained for conditions: (A) Cit/Ca=0 , Q=68 mL.min^{-1}(B) Cit/Ca=0.2 , Q=68 mL.min^{-1} before Maturation (C) Cit/Ca=1.6 , Q=68 mL.min^{-1} after maturation (D) Cit/Ca=0 , Q=15 mL.min^{-1}, obtained from a previous study. Magnification of 100 000 x.

Unfortunately, it was not possible to obtain clear images, due to the presence of large "blocks" of aggregates and the small size of the formed particles and the small size of the formed particles. These aggregates do not represent the behaviour/state of the suspended particles in the solution. They were more likely to be formed during the filtration and drying processes of the collected suspensions. However, in Figure 21 B and C it is still possible to notice the contour of individualized particles in the aggregates boundary. Some of these particles were measured with the Fiji image software and it was possible to observe differences in the particle sizes compared to the images obtained in a previous work (Figure 21 D), where the HAp production was performed without citrate addition. The particles measured in the Figure 21 C varies between 2 and 5 nm in width and 6 and 22 nm in length, while the particles from Figure 21 D varies between 14 and 20 nm in width and 23 and 59 nm in length. These results suggest that the presence of citrate may

have promoted the formation of smaller elongated particles. However, the poor quality of the images obtained does not allow for any conclusions to be drawn.

Considering the potential of the results, the samples will be analysed again. However, the results will not be available in time for the provisional delivery of this document. Yet, they will be discussed during the public defence of this thesis. For this new analysis, the grains of the dried samples will be macerated in order to promote the particle disaggregation. In addition, given that the suspension consists mainly of water and particles, the content of one microdot (corresponding to the same samples) will be directly resuspended in ethanol and immediately analysed, in order to minimise the effects caused by the previous methodology (filtration and drying procedures) and to obtain the most accurate representation of the suspended particles.

4.2. Continuous synthesis of HAp in the large reactor

The maximum flow rate that can be used to ensure good mixing efficiency in each of the smallest reactor cells was already explored in section 4.1. As a result, to increase the production even further, an evaluation of the effect of Cit/Ca ratio on particle dispersion took place, in a larger reactor with the same typology (see Materials). The samples were characterized similarly, as well.

4.2.1. Final pH and production rate

The powders obtained from each of the Cit/Ca experiments were weighted, to estimate the production yields and the production rate. The final pH values were also measured in the collected suspensions and the overall results are listed in Table 4.

Table 4 - Final pH value, crystals production rate ($g.h^{-1}$) and yield for each studied condition of flow rate, Q ($mL.min^{-1}$) and Cit/Ca molar ratio.

.

Q ($mL.min^{-1}$)	Cit/Ca	pH	Yield (%)	Production Rate ($g.h^{-1}$)
135	**0.0**	12.1	-	-
	0.2	12.0	46.1	93.40
	1.6	12.0	58.7	118.9

The results obtained in this section were similar to those already discussed in section 4.1.1. The final pH proved to be high enough (~12.0) to favour the formation of HAp. With this flow rate (135 $mL.min^{-1}$) a production rate of 203 $g.h^{-1}$ should be expected. However it was not possible to achieve these values due to yields around 50%. Moreover, these results could be influenced by the methodology used to get the dry samples, as described in 4.1.1. Despite the low yields, it was still possible to successfully increase the production from 23 $g.h^{-1}$, in a previous work [7], to about 100 $g.h^{-1}$.

4.2.2. Phase identification

In order to confirm the formation of an apatite phase in the scale-up reactor, the functional group analysis (FTIR) and the calcium phosphorus (Ca/P) molar ratio were determined.

4.2.2.1. **Functional group analysis**

The FTIR spectra obtained from each Cit/Ca ratio, before and after maturation time, is represented in Figure 22 as well as a spectrum of a commercial HAp as reference. The functional group peak positions obtained for each spectrum were also summarized in the table A1.1 of the Appendix 1.

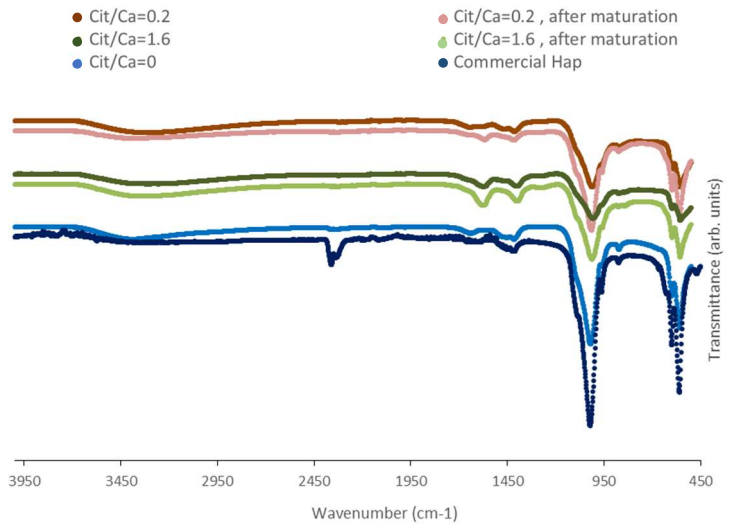

Figure 22 - FTIR spetra corresponding to the particles synthesized with different Cit/Ca ratios, before and after maturation, and comparison with a commercial Hap spectrum (900203, Sigma Aldrich).

Both in the presence and in the absence of citrate, it was possible to identify most of the peaks corresponding to the characteristic functional groups of HAp, as already discussed in section 4.1.2.1. The peaks attributed to the antisymmetric and to the

symmetric stretching modes of carboxyl groups coordinated with the Ca^{2+} on the HAp surface were also identified in the positions between 1574-1567 cm^{-1} and 1396-4017 cm^{-1} respectively. The difference between the antisymmetric and the symmetric vibrations obtained in this reactor corroborate the results reported in the smaller reactor. Once more, the citrate concentration tends to affect the nature of the interaction between the carboxyl group from citrate and the Ca^{2+} from the particle surface, changing from a ionic interaction (Cit/Ca=0.2) to a pseudo-bridging interaction (Cit/Ca=1.6). In summary, the scale-up of the reactor did not reveal significant changes in the apatite phase obtained, neither in the type of interactions occurring on the particles surface.

4.2.2.2. **Ca/P molar ratio**

For the scale-up reactor only one sample was analyzed, corresponding to the conditions: Q=135 $mL.min^{-1}$ and Cit/Ca=1.6 after maturation. It was not possible to produce the desirable apatite phase. A Ca/P=1.39 was obtained for this condition, a similar value already reported for the smaller reactor in the same conditions. The results obtained in this section corroborates the explanation discussed in section 4.1.2.2 since the residence time in this reactor was considered low (28 seconds). Generally, it seems that it was possible to scale-up the reactor without changing the Ca/P molar ratio of the particles produced.

4.2.3. Effect of citrate on particle size distributions

The particle size distributions were also analysed in the scale-up reactor to verify the effect of citrate on particle dispersion in a larger volume reactor. Figure 23 shows the particle size distributions for three Cit/Ca molar ratios, along several days of maturation. Regardless of the citrate ratio, at the exit of the reactor (0 days), particles at the micrometric scale were always obtained. These results were already expected considering the high flow rate (135 $mL.min^{-1}$) used and the results reported from the small reactor.

When it comes to the ratio of Cit/Ca=0.2 (Figure 23 B), it was possible to observe a displacement of the particle size distribution to smaller sizes, after one day of maturation. However, the particles dispersion was not enough since the particle size distributions remained constant in the micrometric scale for the next 30 days.

Regarding the ratio of Cit/Ca=1.6 (Figure 23 C) allowed the production of particles with size distributions on the nanoscale. However, the citrate action in this reactor was slower than in the previous one. It needed a longer maturation time to obtain particles

within the required size. This could be related to differences in reactor size and material, or it could be due to the increase in flow rate.

In general, the results from both reactors, seem to suggest a relation between the flow rate value and the maturation time required to disperse the nanoparticles. However, due to time constraints, it was not possible to conduct additional tests to further investigate this correlation.

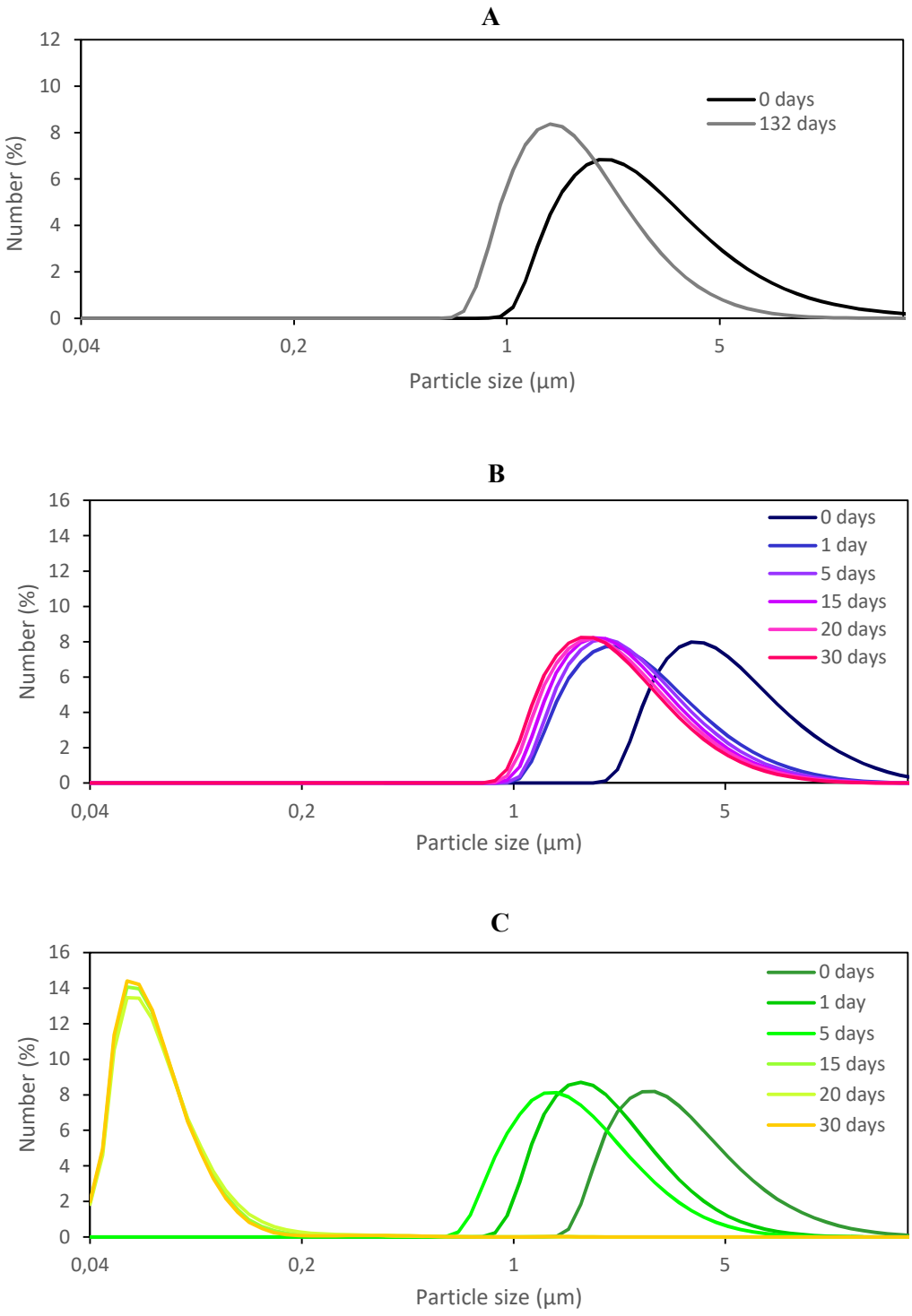

Figure 23 - Particle size distribution, in number, obtained after different maturation times, from the particles synthesized with the following Cit/Ca ratios: (A) Cit/Ca=0 , (B) Cit/Ca=0.2 and (C) Cit/Ca=1.6.

4.2.4. Effect of citrate on suspension stability (Zeta Potential)

The results of the zeta potential obtained for this reactor are presented in Figure 24. Similar to what was discussed in section 4.1.4 for the small reactor, values of zeta potential close to -30 mV were also obtained in this reactor, for both Cit/Ca ratios studied. These results corroborate what was reported by Pochapski et al., [98], which in the presence of aggregates zeta potential may not be the best analysis for determining the stability of the suspension.

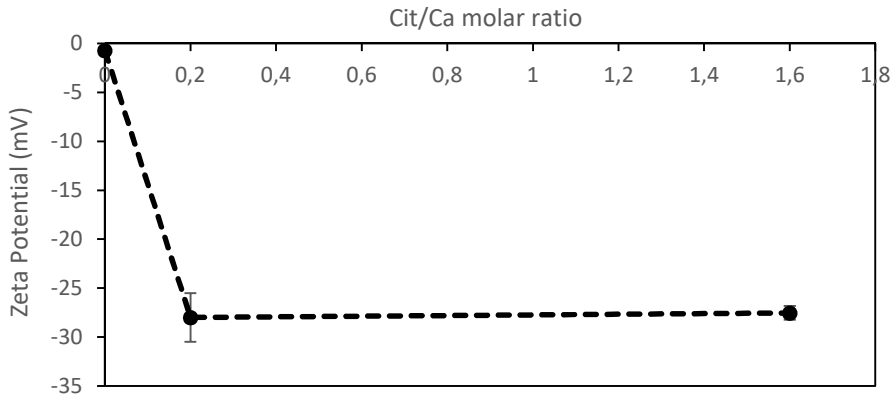

Figure 24- Zeta potentials of the particles produced with different Cit/Ca ratios.

5. Conclusions

In this work, the continuous crystallization/precipitation of HAp nanoparticles in a planar-OFR was performed to evaluate the effect of citrate concentration on particle dispersion, in order to overcome the aggregation problem previously reported, so that nanoparticles with a precise controlled size (<100nm) and a narrow size distribution could be obtained, meeting the specific requirements for drug delivery applications. This effect was also evaluated in a scale-up reactor with the aim of increasing the production rate.

This study confirmed the potential of citrate as a powerful tool to disperse the nanoparticles during its synthesis in a meso-OFR. However, it was possible to conclude that the flow rate and the residence time plays a significant role in the particle aggregation and in the apatite phase formation, respectively.

The presence of adsorbed citrate on the surface of the particles was confirmed by functional group analysis. The increase of the Cit/Ca ratio led to changes in the mode of interaction between the carboxyl group of citrate and the calcium ion of Hap.

In general, the ratio of Cit/Ca=1.6 demonstrated to be the most efficient condition for particle dispersion, given the ability to obtain particle size distributions in the nanometric range, in the shortest amount of time, while the ratio of Cit/Ca=0.2 was found to be an insufficient amount of citrate for an effective particle dispersion. However, the results shown that the effect of citrate on particle dispersion was not instantaneous. There was a required maturation timeframe for the citrate molecules to be adsorbed onto the HAp surface. According to this study, increasing the production rate (by increasing flow rate or Scale up the reactor) results in longer maturation times to get the same results (nanoparticles), since higher flow rates (with higher energy) may improve the mixing in the reactor channels, increasing particle interaction and so their tendency to aggregate.

The images obtained by TEM evidence that the presence of citrate may have promoted the formation of elongated particles even smaller and then the results reported by the laser diffraction analysis, which corroborate the mechanism of citrate adsorption onto the Hap surface reported in literature. This study also corroborated that in the presence of aggregates instead of individualized particulates, a high zeta potential value may be erroneously obtained, which do not necessarily reflect high colloidal stability.

The low values obtained for the Ca/P ratio proved that it was not possible to produce the desired apatite phase in any of the conditions. Instead, intermediate phases of the Hap formation appear to have been produced, such as brushite and monenite. However, the phase determination are more related to the residence time, due to the increase in the flow rate, rather than the presence of citrate molecules. As a result, the study of citrate as a surfactant agent in the synthesis of dispersed HAp nanoparticles remains a strategy with high potential. The scale-up of the reactor did not reveal significant changes in the apatite phase obtained, neither in the suspension stability nor in the type of interactions occurring on the HAp surface.

5.1. Limitations and Future Work

This thesis was limited by the time available for its development and the availability of analytical techniques that allowed for a better assessment of the results within the limited timeframe available. Throughout result discussion it was possible to identify several future works that must be explored to confirm and evaluate some of the proposals made across the discussion.

The ratio of Cit/Ca=1.6 demonstrated to be the most efficient condition for particle dispersion, given the ability to obtain particle size distributions in the nanometric range, in the shortest amount of time. However, since only two Cit/Ca were evaluated (Cit/Ca=0.2 and 1.6) an intermediate Cit/Ca ratio should also be tested in a future work to assess whether the same effect may be obtained with less citrate concentration, hence minimizing contaminations. The particle size results of both reactors, seem to suggest a relationship between the flow rate value and the maturation time required to disperse the nanoparticles. Aditional studies should be conducted to further investigate this correlation.

The Ca/P molar ratio results show the formation of other calcium phosphates instead of HAp in all conditions. A more detailed examination raised questions regarding the role of the residence time in the formation of the apatite phase. These results were the last to be obtained, therefore, there was no time to repeat the tests maintaining the residence time of the previous work. Yet, further studies should be conducted to assess the effect of residence time on the apatite phase formation. Reminding that, after optimization of the residence time parameter, the present study should be repeated (in a system that favours the production of HAp) to confirm that the increase of Ca/P caused by the presence of

citrate does not exceed the regulated values of the production of HAp set by the European Union and the United States of America.

The FTIR analysis also revealed different types of interactions between the carboxyl group of citrate molecules and the calcium ion of HAp which may be an interesting research area to further explore the citrate mechanism of action on particle dispertion.

6. Bibliography

[1] P. Crafts, “The Role of Solubility Modeling and Crystallization in the Design of Active Pharmaceutical Ingredients,” 2007.

[2] Q. Shi, H. Chen, Y. Wang, J. Xu, Z. Liu, and C. Zhang, “Recent advances in drug polymorphs: Aspects of pharmaceutical properties and selective crystallization,” *International Journal of Pharmaceutics*, vol. 611, Jan. 2022,

[3] C. J. Testa *et al.*, “Heterogeneous Crystallization as a Process Intensification Technology in an Integrated Continuous Manufacturing Process for Pharmaceuticals,” *Organic Process Research and Development*, vol. 25, no. 2, pp. 225–238, Feb. 2021,

[4] D. A. Green, “Crystallizer mixing: Understanding and modeling crystallizer mixing and suspension flow,” in *Handbook of Industrial Crystallization*, Cambridge University Press, 2019, pp. 290–312.

[5] T. Mcglone, N. E. B. Briggs, C. A. Clark, C. J. Brown, J. Sefcik, and A. J. Florence, “Oscillatory Flow Reactors (OFRs) for Continuous Manufacturing and Crystallization,” 2015,

[6] Y. Ma, S. Wu, E. G. J. Macaringue, T. Zhang, J. Gong, and J. Wang, “Recent Progress in Continuous Crystallization of Pharmaceutical Products: Precise Preparation and Control,” *Organic Process Research and Development*, vol. 24, no. 10, pp. 1785–1801, Oct. 2020,

[7] J. Machado, “Continuous synthesis of hydroxyapatite nanoparticles in a planar oscillatory flow reactor,” Porto, Feb. 2022.

[8] A. Myerson, *Handbook of Industrial Crystallization*, Second. Elsevier, 2002.

[9] L. Yu and S. M. Reutzel-Edens, “Crystallization - Basic principles,” in *Encyclopedia of Food Sciences and Nutrition*, Second., Academic Press, 2003, pp. 1697–1702.

[10] C. Oliveira, “Precipitação do fosfato dicálcico: caracterização experimental e modelização,” Universidade do Porto, Porto, 2007.

[11] B. Guo, S. Song, A. Ghalambor, and T. R. Lin, “Flow Assurance,” in *Offshore Pipelines*, Second., Gulf Professional Publishing, 2014, pp. 179–231.

[12] A. M. Schwartz and A. S. Myerson, “Solutions and solution properties,” 2002.

[13] J. W. Mullin, *Crystallization*. 2001.

[14] P. Cruz, "Aplicação de um novo reator de fluxo oscilatório no controlo da qualidade e tamanho dos cristais de paracetamol."

[15] J. W. Mullin, "Nucleation," in *Crystallization*, 4th ed., Butterworth-Heinemann, 2001, pp. 181–215.

[16] F. Castro, "Process Intensification for the Production of Hydroxyapatite Nanoparticles," Universidade do Minho, 2013.

[17] J. F. Richardson, J. H. Harker, and J. R. Backhurst, "Crystallisation," in *Chemical Engineering*, 5th ed., vol. 2, Butterworth-Heinemann, 2002, pp. 827–900.

[18] D. Erdemir, A. Y. Lee, and A. S. Myerson, "Nucleation of crystals from solution: Classical and two-step models," *Accounts of Chemical Research*, vol. 42, no. 5, pp. 621–629, May 2009,

[19] P. G. Vekilov, "The two-step mechanism of nucleation of crystals in solution," *Nanoscale*, vol. 2, no. 11, pp. 2346–2357, Nov. 2010,

[20] S. D. Thakore, A. Sood, and A. K. Bansal, "Emerging role of primary heterogeneous nucleation in pharmaceutical crystallization," *Drug Development Research*, vol. 81, no. 1, pp. 3–22, Feb. 2020,

[21] S. Xu, Y. Wang, Z. Hou, and X. Chuai, "Overview of secondary nucleation: From fundamentals to application," *Industrial and Engineering Chemistry Research*, vol. 59, no. 41, pp. 18335–18356, Oct. 2020,

[22] L. Bosetti, B. Ahn, and M. Mazzotti, "Secondary Nucleation by Interparticle Energies. I. Thermodynamics," *Crystal Growth and Design*, vol. 22, no. 1, pp. 87–97, Jan. 2022,

[23] K. Tsukamoto, "In Situ Observation of Crystal Growth and Flows by Optical Techniques," in *Handbook of Crystal Growth: Second Edition*, vol. 1, Elsevier Inc., 2015, pp. 1031–1060.

[24] J. J. de Yoreo and P. G. Vekilov, "Principles of Crystal Nucleation and Growth."

[25] J. Dalmolen, "Synthesis and application of new chiral amines in Dutch resolution." [Online]. Available: http://www.rug.nl/research/portal.

[26] P. Duchstein, P. Ectors, and D. Zahn, "Molecular simulations of crystal growth: From understanding to tailoring," in *Advances in Inorganic Chemistry*, vol. 73, Academic Press Inc., 2019, pp. 507–529.

[27] S. S. Joshi, “Crystal Habit Modification Using Habit Modifiers.” [Online]. Available: www.intechopen.com

[28] M. R. Prasad, P. K. Deb, B. Chandrasekaran, R. Maheshwari, and R. K. Tekade, “Basics of Crystallization Process Applied in Drug Exploration,” in *Dosage Form Design Parameters*, vol. 2, Elsevier, 2018, pp. 67–103.

[29] M. M. Bommana, B. Kirthivasan, S. S. Gupta, A. Shikhar, and A. Shah, “Nanostructures in pharma: Elixir to oral medicine,” in *Nanoparticles in Pharmacotherapy*, Elsevier, 2019, pp. 23–44.

[30] A. Lewis, M. M. Seckler, H. Kramer, and G. van Rosmalen, “Agglomeration,” in *Industrial Crystallization*, Cambridge: Cambridge University Press, 2015, pp. 130–150.

[31] E. Simone, R. Othman, G. T. Vladisavljević, and Z. K. Nagy, “Preventing Crystal Agglomeration of Pharmaceutical Crystals Using Temperature Cycling and a Novel Membrane Crystallization Procedure for Seed Crystal Generation,” *Pharmaceutics*, vol. 10, no. 1, Mar. 2018,

[32] M. Tourbin *et al.*, “Agglomeration of stoichiometric hydroxyapatite: Impact on particle size distribution and purity in the precipitation and maturation steps,” *Powder Technology*, vol. 360, pp. 977–988, Jan. 2020,

[33] D. Zhang, S. Xu, S. Du, J. Wang, and J. Gong, “Progress of Pharmaceutical Continuous Crystallization,” *Engineering*, vol. 3, no. 3, pp. 354–364, Jun. 2017,

[34] Horiba instruments, “A guidebook to particle size analysis,” 2019.

[35] M. Baumber, “The Importance of Particle Size Distribution in Pharmaceuticals,” Apr. 01, 2020. https://www.quadro-mpt.com/news-and-events/the-importance-of-particle-size-distribution-in-pharmaceuticals (accessed Feb. 07, 2022).

[36] M. Torbacke and A. S. K. C. Rasmuson, “Infuence of diferent scales of mixing in reaction crystallization,” *Chemical Engineering Science* , vol. 56, pp. 2459–2473, 2001.

[37] D. Maximilian Besenhard Graz, “Continuous Crystallization of Active Pharma-ceutical Ingredients via a Tubular Reactor: Simulation and Process Design.”

[38] S. D. Schaber, D. I. Gerogiorgis, R. Ramachandran, J. M. B. Evans, P. I. Barton, and B. L. Trout, “Economic analysis of integrated continuous and batch pharmaceutical manufacturing: A case study,” *Industrial and Engineering Chemistry Research*, vol. 50, no. 17. pp. 10083–10092, Sep. 07, 2011.

[39] P. Cruz, C. Silva, F. Rocha, and A. Ferreira, “The axial dispersion of liquid solutions and solid suspensions in planar oscillatory flow crystallizers,” *AIChE Journal*, vol. 65, no. 9, Sep. 2019,

[40] P. Cruz, C. Silva, F. Rocha, and A. Ferreira, “Mixing performance of planar oscillatory flow reactors with liquid solutions and solid suspensions,” *Industrial and Engineering Chemistry Research*, vol. 60, no. 6, pp. 2663–2676, Feb. 2021,

[41] M. Koyama, S. Kudo, S. Amari, and H. Takiyama, “Development of novel cascade type crystallizer for continuous production of crystalline particles,” 2020,

[42] P. Bianchi, J. D. Williams, and C. O. Kappe, “Oscillatory flow reactors for synthetic chemistry applications,” *Journal of Flow Chemistry*, vol. 10, no. 3, pp. 475–490, Sep. 2020,

[43] A. P. Harvey, M. R. Mackley, and P. Stonestreet, “Operation and Optimization of an Oscillatory Flow Continuous Reactor,” 2001,

[44] F. Castro, A. Ferreira, F. Rocha, A. Vicente, and J. A. Teixeira, “Continuous-flow precipitation of hydroxyapatite at 37 °c in a meso oscillatory flow reactor,” *Industrial and Engineering Chemistry Research*, vol. 52, no. 29, pp. 9816–9821, Jul. 2013,

[45] M. Schoenitz, L. Grundemann, W. Augustin, and S. Scholl, “Fouling in microstructured devices: a review,” *Chemical Communications*, vol. 51, no. 39, pp. 8213–8228, Apr. 2015,

[46] N. E. B. Briggs, U. Schacht, V. Raval, T. McGlone, J. Sefcik, and A. J. Florence, “Seeded Crystallization of β- L -Glutamic Acid in a Continuous Oscillatory Baffled Crystallizer,” *Organic Process Research and Development*, vol. 19, no. 12, pp. 1903–1911, Dec. 2015,

[47] A. Mazubert, D. F. Fletcher, M. Poux, and J. Aubin, “Hydrodynamics and mixing in continuous oscillatory flow reactors—Part I: Effect of baffle geometry,” *Chemical Engineering and Processing: Process Intensification*, vol. 108, pp. 78–92, Oct. 2016,

[48] A. Ferreira, F. Rocha, J. A. Teixeira, and F. Castro, “Modular oscillatory flow plate reactor,” WO2017175207A1, Oct. 12, 2017

[49] P. Cruz, F. Rocha, and A. Ferreira, “Crystallization of paracetamol from mixtures of ethanol and water in a planar oscillatory flow crystallizer: effect of the oscillation conditions on the crystal growth kinetics,” *CrystEngComm*, vol. 23, no. 47, pp. 8301–8314, 2021,

[50] N. Reis, A. A. Vicente, J. A. Teixeira, and M. R. Mackley, “Residence times and mixing of a novel continuous oscillatory flow screening reactor,” *Chemical Engineering Science*, vol. 59, no. 22–23, pp. 4967–4974, Nov. 2004,

[51] P. Cruz, F. Rocha, and A. Ferreira, “Effect of operating conditions on batch and continuous paracetamol crystallization in an oscillatory flow mesoreactor,” *CrystEngComm*, vol. 18, no. 47, pp. 9113–9121, 2016,

[52] P. Cruz, F. Rocha, and A. Ferreira, “Crystallization of paracetamol from aqueous solutions in a planar oscillatory flow crystallizer: effect of the oscillation conditions on the nucleation kinetics,” *CrystEngComm*, vol. 23, no. 39, pp. 6930–6941, Oct. 2021,

[53] S. Lawton, G. Steele, P. Shering, L. Zhao, I. Laird, and X. W. Ni, “Continuous crystallization of pharmaceuticals using a continuous oscillatory baffled crystallizer,” *Organic Process Research and Development*, vol. 13, no. 6, pp. 1357–1363, Nov. 2009,

[54] F. J. Keil, “Process intensification,” *Reviews in Chemical Engineering*, vol. 34, no. 2, pp. 135–200, Mar. 2018,

[55] Y. Tian, S. E. Demirel, M. M. F. Hasan, and E. N. Pistikopoulos, “An overview of process systems engineering approaches for process intensification: State of the art,” *Chemical Engineering and Processing - Process Intensification*, vol. 133, pp. 160–210, Nov. 2018,

[56] A. Chakrabarty, S. Mannan, and T. Cagin, “Multiscale Modeling for Process Safety Applications,” *Multiscale Modeling for Process Safety Applications*, pp. 1–429, Dec. 2015,

[57] S. Fernando, M. McEnery, and S. A. Guelcher, “Polyurethanes for bone tissue engineering,” *Advances in Polyurethane Biomaterials*, pp. 481–501, Jan. 2016,

[58] J. H. Kim, S. H. Kim, H. K. Kim, T. Akaike, and S. C. Kim, “Synthesis and characterization of hydroxyapatite crystals: a review study on the analytical methods,” *J Biomed Mater Res*, vol. 62, no. 4, pp. 600–612, Dec. 2002,

[59] A. Haider, S. Haider, S. S. Han, and I. K. Kang, “Recent advances in the synthesis, functionalization and biomedical applications of hydroxyapatite: a review,” *RSC Advances*, vol. 7, no. 13, pp. 7442–7458, Jan. 2017,

[60] E. Andronescu *et al.*, “Nano-hydroxyapatite: Novel approaches in biomedical applications,” in *Nanobiomaterials in Hard Tissue Engineering: Applications of Nanobiomaterials*, Elsevier Inc., 2016, pp. 189–213.

[61] K. Lin and J. Chang, “Structure and properties of hydroxyapatite for biomedical applications,” in *Hydroxyapatite (Hap) for Biomedical Applications*, Elsevier, 2015, pp. 3–19.

[62] J. Kamieniak, P. J. Kelly, C. E. Banks, and A. M. Doyle, “Mechanical, pH and Thermal Stability of Mesoporous Hydroxyapatite,” *Journal of Inorganic and Organometallic Polymers and Materials*, vol. 28, no. 1, pp. 84–91, Jan. 2018,

[63] W. Li, F. Han, H. Liu, X. Niu, and L. Shi, “The synthesis of sulfate doped hydroxyapatite for enhanced drug loading and chemotherapeutic drug delivery towards lung cancer treatment,” *Ceramics International*, vol. 46, no. 18, pp. 28578–28584, Dec. 2020,

[64] Y. Liu *et al.*, “Sustained and controlled delivery of doxorubicin from an in-situ setting biphasic hydroxyapatite carrier for local treatment of a highly proliferative human osteosarcoma,” *Acta Biomaterialia*, vol. 131, pp. 555–571, Sep. 2021,

[65] S. Mondal, S. v. Dorozhkin, and U. Pal, “Recent progress on fabrication and drug delivery applications of nanostructured hydroxyapatite,” *Wiley Interdisciplinary Reviews: Nanomedicine and Nanobiotechnology*, vol. 10, no. 4, pp. 1–32, 2018,

[66] S. Lara-Ochoa, W. Ortega-Lara, and C. E. Guerrero-Beltrán, “Hydroxyapatite nanoparticles in drug delivery: Physicochemistry and applications,” *Pharmaceutics*, vol. 13, no. 10, pp. 1–24, 2021,

[67] G. Singh, • Ravinder, P. Singh, • Sukhwinder, S. Jolly, and G. Abstract, “Customized hydroxyapatites for bone-tissue engineering and drug delivery applications: a review,” *Journal of Sol-Gel Science and Technology*, vol. 94, pp. 505–530, 2020,

[68] G. Tiwari *et al.*, “Drug delivery systems: An updated review,” *Int J Pharm Investig*, vol. 2, no. 1, p. 2, 2012,

[69] I. Rodríguez-Ruiz *et al.*, “PH-responsive delivery of doxorubicin from citrate-apatite nanocrystals with tailored carbonate content,” *Langmuir*, vol. 29, no. 26, pp. 8213–8221, Jul. 2013,

[70] M. Sadat-Shojai, M. T. Khorasani, E. Dinpanah-Khoshdargi, and A. Jamshidi, “Synthesis methods for nanosized hydroxyapatite with diverse structures,” *Acta Biomater*, vol. 9, no. 8, pp. 7591–7621, 2013,

[71] D. S. Gomes, A. M. C. Santos, G. A. Neves, R. R. Menezes, C. Grande, and C. Grande, “A brief review on hydroxyapatite production and use in biomedicine (Uma breve revisão sobre a obtenção de hidroxiapatita e aplicação na biomedicina),” *Cerâmica*, vol. 65, pp. 282–302, 2019.

[72] C. Liu, Y. Huang, W. Shen, and J. Cui, “Kinetics of hydroxyapatite precipitation at pH 10 to 11,” 2001.

[73] A. Ferreira, C. Oliveira, and F. Rocha, “The different phases in the precipitation of dicalcium phosphate dihydrate,” *Journal of Crystal Growth*, vol. 252, no. 4, pp. 599–611, May 2003,

[74] A. Yelten-Yilmaz and S. Yilmaz, “Wet chemical precipitation synthesis of hydroxyapatite (HA) powders,” *Ceramics International*, vol. 44, no. 8, pp. 9703–9710, Jun. 2018,

[75] H. Heinz *et al.*, “Nanoparticle decoration with surfactants: Molecular interactions, assembly, and applications,” *Surface Science Reports*, vol. 72, no. 1, pp. 1–58, Feb. 2017,

[76] C. Santos, “Synthesis and funtionalization of Hydroxyapatite nanoparticles,” Universidade de Aveiro, 2012.

[77] Y. Xiong, P. Tan, Q. Liu, K. Liu, and J. Tan, “Aqueous Preparation of Highly Dispersed Hydroxyapatite Nanorods for Colloidal Liquid Crystals,” *Journal of Wuhan University of Technology-Mater. Sci. Ed. 2021 36:2*, vol. 36, no. 2, pp. 230–238, Jul. 2021,

[78] D. correia, “Production of Hydroxyapatite Nanoparticles for Cosmetic and Orthopaedic Applications: Effect of Chelants and Dispersants,” 2008.

[79] L. Pastero, M. Bruno, and D. Aquilano, “Habit change of monoclinic hydroxyapatite crystals growing from aqueous solution in the presence of citrate ions: The role of 2D epitaxy,” *Crystals (Basel)*, vol. 8, no. 8, Aug. 2018,

[80] S. H. Daryan, A. Khavandi, and J. Javadpour, “Surface engineered hollow hydroxyapatite microspheres: Hydrothermal synthesis and growth mechanisms,” *Solid State Sciences*, vol. 106, p. 106301, Aug. 2020,

[81] X. Jin, J. Zhuang, Z. Zhang, H. Guo, and J. Tan, “Hydrothermal synthesis of hydroxyapatite nanorods in the presence of sodium citrate and its aqueous colloidal stability evaluation in neutral pH,” *Journal of Colloid and Interface Science*, vol. 443, pp. 125–130, Apr. 2015,

[82] M. A. Martins, C. Santos, M. M. Almeida, and M. E. v. Costa, “Hydroxyapatite micro- and nanoparticles: Nucleation and growth mechanisms in the presence of citrate species,” *Journal of Colloid and Interface Science*, vol. 318, no. 2, pp. 210–216, Feb. 2008,

[83] C. Santos, M. M. Almeida, and M. E. Costa, “Morphological Evolution of Hydroxyapatite Particles in the Presence of Different Citrate:Calcium Ratios,” *Crystal Growth and Design*, vol. 15, no. 9, pp. 4417–4426, Sep. 2015,

[84] H. Yang, L. Hao, C. Du, and Y. Wang, “A systematic examination of the morphology of hydroxyapatite in the presence of citrate,” *RSC Advances*, vol. 3, no. 45, pp. 23184–23189, Dec. 2013,

[85] W. Jiang *et al.*, “Atomic force microscopy reveals hydroxyapatite-citrate interfacial structure at the atomic level,” *Langmuir*, vol. 24, no. 21, pp. 12446–12451, Nov. 2008,

[86] L. Degli Esposti, A. Adamiano, D. Siliqi, C. Giannini, and M. Iafisco, “The effect of chemical structure of carboxylate molecules on hydroxyapatite nanoparticles. A structural and morphological study,” *Bioactive Materials*, vol. 6, no. 8, pp. 2360–2371, Aug. 2021,

[87] G. Verma, K. C. Barick, N. G. Shetake, B. N. Pandey, and P. A. Hassan, “Citrate-functionalized hydroxyapatite nanoparticles for pH-responsive drug delivery,” *RSC Advances*, vol. 6, no. 81, pp. 77968–77976, 2016,

[88] N. Salahuddin, E. Ibrahim, and M. El-Kemary, “Surfactant free-poly(lactic-co-glycolic acid) coated artesunate loaded citrate-functionalized hydroxyapatite nanorods as a nanocapsule for improving artesunate delivery and antitumor efficiency,” *Ceramics International*, Jan. 2022,

[89] Beckman Coulter, “Coulter Principle Short Course.” pp. 1–19.

[90] P. Senthil Kumar, K. Grace Pavithra, and M. Naushad, “Characterization techniques for nanomaterials,” in *Nanomaterials for Solar Cell Applications*, Elsevier, 2019, pp. 97–124.

[91] H. S. Vilela, M. C. Rodrigues, B. M. Fronza, R. B. Trinca, F. M. Vichi, and R. R. Braga, “Effect of Temperature and pH on Calcium Phosphate Precipitation,” *Crystal Research and Technology*, vol. 56, no. 12, Dec. 2021,

[92] L. C. Chow, “Next generation calcium phosphate-based biomaterials,” *Dental Materials Journal*, vol. 28, no. 1. pp. 1–10, 2009.

[93] I. Rehman and W. Bonfield, “Characterization of hydroxyapatite and carbonated apatite by photo acoustic FTIR spectroscopy,” *Journal of Materials Science: Materials in Medicine 1997 8:1*, vol. 8, no. 1, pp. 1–4, Jan. 1997,

[94] A. Veiga, F. Castro, C. Reis, A. Sousa, A. L. Oliveira, and F. Rocha, “Hydroxyapatite/sericin composites: A simple synthesis route under near-physiological conditions of temperature and pH and preliminary study of the effect of sericin on the biomineralization process,” *Materials Science and Engineering C*, vol. 108, Mar. 2020,

[95] D. A. Nowicki, J. M. S. Skakle, and I. R. Gibson, “Nano-scale hydroxyapatite compositions for the utilization of CO2 recovered using post-combustion carbon capture,” *Journal of Materials Chemistry A*, vol. 6, no. 13, pp. 5367–5377, 2018,

[96] A. López-Macipe, J. Gómez-Morales, and R. Rodríguez-Clemente, “The Role of pH in the Adsorption of Citrate Ions on Hydroxyapatite,” *Journal of Colloid and Interface Science*, vol. 200, no. 1, pp. 114–120, Apr. 1998,

[97] S. A. Siddiqi and U. Azhar, “Carbonate substituted hydroxyapatite,” *Handbook of Ionic Substituted Hydroxyapatites*, pp. 149–173, Jan. 2020,

[98] D. J. Pochapski, C. Carvalho Dos Santos, G. W. Leite, S. H. Pulcinelli, and C. V. Santilli, “Zeta Potential and Colloidal Stability Predictions for Inorganic Nanoparticle Dispersions: Effects of Experimental Conditions and Electrokinetic Models on the Interpretation of Results,” *Langmuir*, vol. 37, no. 45, pp. 13379–13389, Nov. 2021,

7. Appendix

Appendix 1: Functional groups peak identification for each FTIR spectr

Table A1. 1 - Functional group peak positions and respective identification for each of the conditions tested in this study. v_s: vibrational mode of the symmetric stretching modes of carboxyl groups coordinated to Ca^{2+}. v_{as}: vibrational mode of the antisymmetric stretching modes of carboxyl groups coordinated to Ca^{2+}. **Δv:** difference between the antisymmetric and the symmetric peak positions.

				Hap peaks										Citrate-Hap peaks		
Sample conditions				Hydroxyl stretch	Carbonate v_3 (1650-1300)			Phosphate v_3 (1190-976)		Phosphate v_1	Carbonate v_2	Phosphate v_4 (660-520)			Carboxyl v_{as}	Carboxyl v_s	Δv
Reactor type	Flow rate (mL/min)	Cit/Ca	Maturation (days)	**3570**	**1648**	**1454**	**1419**	**1091**	**1042**	**962**	**877**	**632**	**602**	**566**	**1542-1602**	**1342-1440**	
Small	68	0	0	Band	1644	-	1414	1093	1009	956	871	649	599	555	-	-	-
		0.2	0		-	-	-	-	1012	962	873	-	601	557	1568	1416	152
		0.2	15		-	-	-	1087	1014	961	874	-	600	558	1567	1417	150
		1.6	-		-	-	-	-	-	-	-	-	-	-	-	-	-
		1.6	10		-	-	-	-	1012	961	875	-	600	557	1574	1402	172
	88	0.2	0	Band	-	-	-	-	1011	960	873	-	601	557	1570	1416	154
		0.2	10		-	-	-	-	1015	961	874	-	600	558	1568	1416	152
		1.6	0		-	-	-	-	1011	960	874	-	600	557	1574	1397	177
		1.6	8		-	-	-		1013	961	875	-	600	557	1574	1404	170
Large	135	0	0	Band	1645		1416		1020	961	873		6001	559	-	-	-
		0.2	0		-	-	-	-	1010	960	872	-	600	556	1646	1416	230
		0.2	36						1015	961	875	-	601	559	1567	1417	150
		1.6	0		-	-	-	-	1008	960	872	-	599	555	1576	1397	179
		1.6	32		-	-	-	-	1012	961	875	-	600	557	1574	1396	178

Appendix 2: Particle size distributions inconsistent measurements

The particle size distribution presented in this work were obtained from the mean of three consecutive measurements obtained from the LS 230 by Beckman Coulter. In some cases, the three consecutive measurements results were not consistent. The distributions varied between the microscale and the nanoscale for the same sample, as shown in the example of Figure A2.1. In order to compare and discuss the results, in this situations, the mean of the three measurements were also presented in the graphs, as illustrated in the example of the Figure A2.2. However, it is important to note that this distribution is not representative of a sample with two size populations: primary particles and aggregates (nano and micro). There is an alteration in the size of the "particles" over the course of the measurements due to the formation of aggregates. Probably as a result of the constant shaking that occurs in the equipment during the measurements.

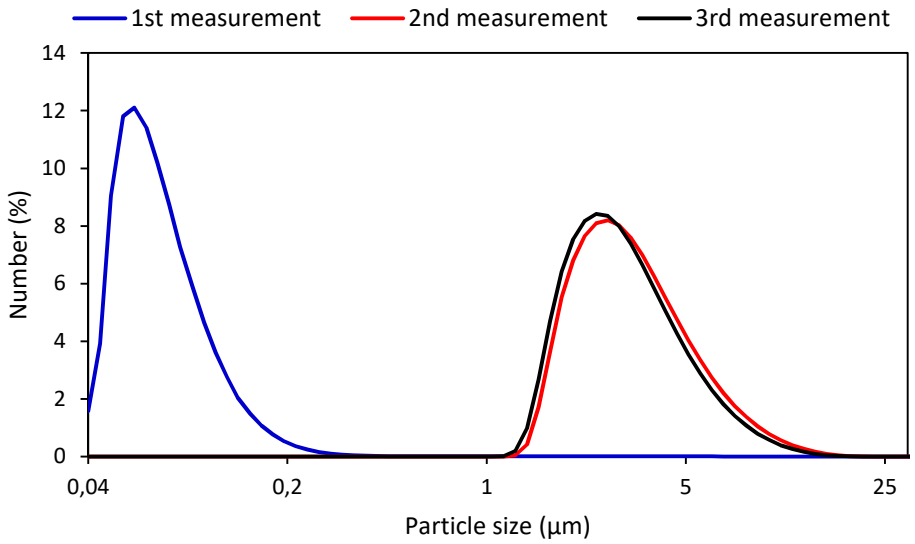

Figure A2. 1 – Particle size distributions of three consecutive inconsistent measurements, example obtained from the conditions: ratio Cit/Ca=0.2, Q=88 mL.min^{-1}.

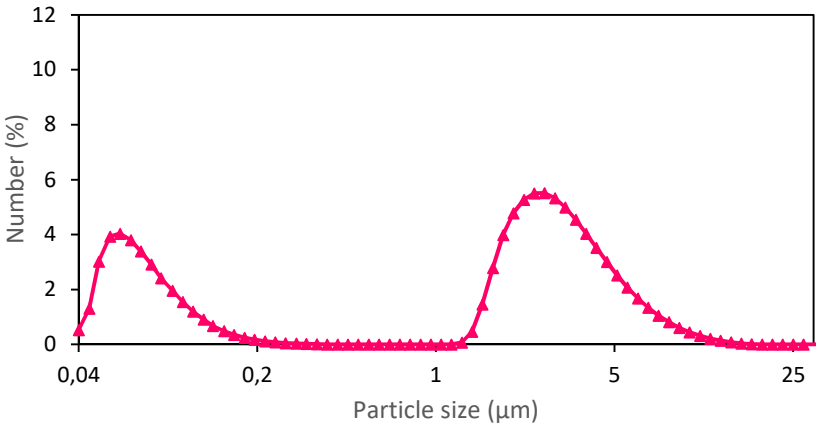

Figure A2. 2- Particle size distribution obtained from the mean of three consecutive inconsistent measurements for the conditions: ratio Cit/Ca=0.2, Q=88 mL.min^{-1}.